

Code-Verification Techniques for the Method-of-Moments Implementation of the Combined-Field Integral Equation

Brian A. Freno^a, Neil R. Matula^a

^a*Sandia National Laboratories, Albuquerque, NM 87185*

Abstract

Code verification plays an important role in establishing the credibility of computational simulations by assessing the correctness of the implementation of the underlying numerical methods. In computational electromagnetics, the numerical solution to integral equations incurs multiple interacting sources of numerical error, as well as other challenges, which render traditional code-verification approaches ineffective. In this paper, we provide approaches to separately measure the numerical errors arising from these different error sources for the method-of-moments implementation of the combined-field integral equation. We demonstrate the effectiveness of these approaches for cases with and without coding errors.

Keywords: method of moments, combined-field integral equation, code verification, manufactured solutions

1. Introduction

For electromagnetic scatterers, Maxwell's equations, together with appropriate boundary conditions, may be formulated as surface integral equations (SIEs). The most common SIEs for modeling time-harmonic electromagnetic phenomena are the electric-field integral equation (EFIE), which relates the surface current to the scattered electric field, and the magnetic-field integral equation (MFIE), which relates the surface current to the scattered magnetic field. The EFIE arises from the condition that the total tangential electric field on the surface of a perfect electric conductor is zero, whereas the MFIE arises from the condition that the component of the total magnetic field tangent to the surface of a perfect electric conductor is equal to the surface current density. At certain frequencies, the accuracy of the solutions to the EFIE and MFIE deteriorates due to the internal resonances of the scatterer. Therefore, the combined-field integral equation (CFIE), which is a linear combination of the EFIE and MFIE, is employed to overcome this problem.

These SIEs are typically solved through the method of moments (MoM), wherein the surface of the electromagnetic scatterer is discretized using planar or curvilinear mesh elements, and four-dimensional integrals are evaluated over two-dimensional source and test elements. These integrals contain a Green's function, which yields singularities when the test and source elements share one or more edges or vertices, and near-singularities when they are otherwise close. The accurate evaluation of these integrals is an active research topic, with many approaches being developed to address the (near-)singularity for the inner, source-element integral [1–10], as well as for the outer, test-element integral [11–15].

Code verification plays an important role in establishing the credibility of results from computational physics simulations [16–18] by assessing the correctness of the implementation of the underlying numerical methods. The discretization of differential, integral, or integro-differential equations incurs some truncation error, and thus the approximate solutions produced from the discretized equations will incur an associated discretization error. If the discretization error tends to zero as the discretization is refined, the consistency of the code is verified [16]. This may be taken a step further by examining not only consistency, but the rate at which the error decreases as the discretization is refined, thereby verifying the order of accuracy of the discretization scheme. The correctness of the numerical-method implementation may then be verified by comparing the expected and observed orders of accuracy obtained from numerous test cases with known solutions.

Email address: bafreno@sandia.gov (Brian A. Freno)

To measure the discretization error, a known solution is required to compare with the discretized solution. Exact solutions are generally limited and may not sufficiently exercise the capabilities of the code. Therefore, manufactured solutions [19] are a popular alternative, permitting the construction of arbitrarily complex problems with known solutions. Through the method of manufactured solutions (MMS), a solution is manufactured and substituted directly into the governing equations to yield a residual term, which is added as a source term to coerce the solution to the manufactured solution.

For code verification, integral equations yield an additional challenge. While analytical differentiation is straightforward, analytical integration is not always possible. Therefore, the residual source term arising from the manufactured solution may not be representable in closed form, and its implementation may be accompanied by numerical techniques that carry their own numerical errors. Furthermore, for the EFIE, MFIE, and CFIE, the aforementioned (nearly) singular integrals can further complicate the numerical evaluation of the source term. Therefore, many of the benefits associated with MMS are lost when applied straightforwardly to these integral equations.

There are many examples of code verification in the literature for different computational physics disciplines. These disciplines include aerodynamics [20], fluid dynamics [21–27], solid mechanics [28], fluid–structure interaction [29, 30], heat transfer in fluid–solid interaction [31], multiphase flows [32, 33], radiation hydrodynamics [34], electrostatics [35], electrodynamics [36, 37], magneto-hydrodynamics [38], and ablation [39–43]. For electromagnetic SIEs, code-verification activities that employ manufactured solutions have been limited to the EFIE [44–47] and, more recently, the MFIE [48].

As described in [46, 48], the EFIE and MFIE, and consequently the CFIE, incur numerical error due to curved surfaces being approximated by planar elements (domain-discretization error), the solution being approximated as a linear combination of a finite number of basis functions (solution-discretization error), and the approximate evaluation of integrals using quadrature rules (numerical-integration error).

For the EFIE, Marchand et al. [44, 45] compute the MMS source term using additional quadrature points. Freno et al. [46] manufacture the Green’s function, permitting the numerical-integration error to be eliminated and the solution-discretization error to be isolated. Freno et al. [47] also provide approaches to isolate the numerical-integration error. For the MFIE, Freno and Matula [48] isolate and measure the solution-discretization error and numerical-integration error.

In this paper, we present code-verification techniques for the MoM implementation of the CFIE that isolate and measure the solution-discretization error and numerical-integration error. For curved surfaces, the domain-discretization error cannot be completely isolated or eliminated, but methods are presented in [48] to account for it in the MFIE. These methods can be applied to the CFIE straightforwardly. In this work, we avoid the domain-discretization error by considering only planar surfaces. We isolate the solution-discretization error by approximating the Green’s function in terms of even powers of the distance between the test and source points. Through this approximation, we can evaluate the integrals exactly, thereby avoiding numerical-integration error. The approximated Green’s function differs from the previously manufactured Green’s function [46, 48] by more closely resembling the actual Green’s function with higher-degree polynomials of the distance. We isolate the numerical-integration error by canceling the influence of the basis functions. We perform convergence studies for different wavenumbers and combination parameters to vary the relative weights between the terms in the CFIE within a physically realistic range.

By approximating the Green’s function in terms of even powers of the distance, we avoid the challenges associated with evaluating the aforementioned (nearly) singular integrals. Given the computational expense of computing accurate reference solutions, assessing these integral evaluations is best accomplished through extensive unit testing as complementary code verification. Examples for the EFIE are included in [15, 49].

This paper is organized as follows. In Section 2, we describe the MoM implementation of the CFIE. In Section 3, we describe the challenges of using MMS with the MoM implementation of the CFIE, as well as our approach to mitigating them. In Section 4, we describe our approach to approximating the Green’s function and evaluating integrals containing it. In Section 5, we demonstrate the effectiveness of our approaches for several different configurations with and without coding errors. In Section 6, we summarize this work.

2. The Method-of-Moments Implementation of the Combined-Field Integral Equation

In time-harmonic form, the scattered electric field \mathbf{E}^S and magnetic field \mathbf{H}^S due to induced surface currents on a scatterer can be computed by [50]

$$\mathbf{E}^S(\mathbf{x}) = -(j\omega\mathbf{A}(\mathbf{x}) + \nabla\Phi(\mathbf{x})), \quad (1)$$

$$\mathbf{H}^S(\mathbf{x}) = \frac{1}{\mu}\nabla \times \mathbf{A}(\mathbf{x}), \quad (2)$$

where the magnetic vector potential \mathbf{A} is defined by

$$\mathbf{A}(\mathbf{x}) = \mu \int_{S'} \mathbf{J}(\mathbf{x}')G(\mathbf{x}, \mathbf{x}')dS', \quad (3)$$

and, by employing the Lorenz gauge condition and the continuity equation, the electric scalar potential Φ is defined by

$$\Phi(\mathbf{x}) = \frac{j}{\epsilon\omega} \int_{S'} \nabla' \cdot \mathbf{J}(\mathbf{x}')G(\mathbf{x}, \mathbf{x}')dS'. \quad (4)$$

In (3) and (4), the integration domain $S' = S$ is the closed surface of a perfect electric conductor, where the prime notation is introduced here to distinguish the inner and outer integration domains later in this section. Additionally, \mathbf{J} is the electric surface current density, μ and ϵ are the permeability and permittivity of the surrounding medium, and G is the Green's function

$$G(\mathbf{x}, \mathbf{x}') = \frac{e^{-jkR}}{4\pi R}, \quad (5)$$

where $R = \|\mathbf{R}\|_2$, $\mathbf{R} = \mathbf{x} - \mathbf{x}'$, and $k = \omega\sqrt{\mu\epsilon}$ is the wavenumber.

2.1. The Electric-Field Integral Equation

The total electric field \mathbf{E} is the sum of the incident electric field \mathbf{E}^I , which induces \mathbf{J} , and \mathbf{E}^S . On S , the tangential component of \mathbf{E} is zero, such that

$$\mathbf{E}_t^S = -\mathbf{E}_t^I, \quad (6)$$

where $(\cdot)_t$ denotes the tangential component. Substituting (1) into (6) yields the EFIE at a point on the surface of the scatterer, from which we can compute \mathbf{J} from \mathbf{E}^I :

$$(j\omega\mathbf{A} + \nabla\Phi)_t = \mathbf{E}_t^I. \quad (7)$$

2.2. The Magnetic-Field Integral Equation

The total magnetic field \mathbf{H} is the sum of the incident magnetic field \mathbf{H}^I and \mathbf{H}^S . On S ,

$$\mathbf{n} \times \mathbf{H} = \mathbf{J}, \quad (8)$$

where \mathbf{n} is the unit vector normal to S . Noting that $\nabla \times [\mathbf{J}(\mathbf{x}')G(\mathbf{x}, \mathbf{x}')] = \nabla G(\mathbf{x}, \mathbf{x}') \times \mathbf{J}(\mathbf{x}')$ and

$$\nabla G(\mathbf{x}, \mathbf{x}') = -\nabla' G(\mathbf{x}, \mathbf{x}'), \quad (9)$$

from (2) and (3),

$$\mathbf{H}^S(\mathbf{x}) = \int_{S'} \mathbf{J}(\mathbf{x}') \times \nabla' G(\mathbf{x}, \mathbf{x}')dS'$$

when \mathbf{x} is just outside of S . Therefore, at S ,

$$\mathbf{n} \times \mathbf{H}^S = \lim_{\mathbf{x} \rightarrow S} \mathbf{n} \times \int_{S'} \mathbf{J}(\mathbf{x}') \times \nabla' G(\mathbf{x}, \mathbf{x}')dS' = \frac{1}{2}\mathbf{J} + \mathbf{n} \times \int_{S'} \mathbf{J}(\mathbf{x}') \times \nabla' G(\mathbf{x}, \mathbf{x}')dS', \quad (10)$$

where the final term is evaluated through principal value integration. From (8) and (10) the MFIE at a point on the surface of the scatterer is [51, 52]

$$\frac{1}{2}\mathbf{J} - \mathbf{n} \times \int_{S'} \mathbf{J}(\mathbf{x}') \times \nabla' G(\mathbf{x}, \mathbf{x}')dS' = \mathbf{n} \times \mathbf{H}^I. \quad (11)$$

2.3. The Method of Moments

Inserting (3) and (4) into (7), projecting (7) onto an appropriate space \mathbb{V} containing vector fields that are tangent to S , and integrating by parts yields the variational form of the EFIE: find $\mathbf{J} \in \mathbb{V}$, such that

$$\int_S \mathbf{E}^{\mathcal{I}} \cdot \bar{\mathbf{v}} dS = j\omega\mu \int_S \bar{\mathbf{v}}(\mathbf{x}) \cdot \int_{S'} \mathbf{J}(\mathbf{x}') G(\mathbf{x}, \mathbf{x}') dS' dS - \frac{j}{\epsilon\omega} \int_S \nabla \cdot \bar{\mathbf{v}}(\mathbf{x}) \int_{S'} \nabla' \cdot \mathbf{J}(\mathbf{x}') G(\mathbf{x}, \mathbf{x}') dS' dS \quad (12)$$

for all $\mathbf{v} \in \mathbb{V}$, where the overbar denotes complex conjugation.

We can write (12) more succinctly in terms of a sesquilinear form and inner product:

$$a^{\mathcal{E}}(\mathbf{J}, \mathbf{v}) = b^{\mathcal{E}}(\mathbf{E}^{\mathcal{I}}, \mathbf{v}), \quad (13)$$

where the sesquilinear form and inner product are defined by

$$\begin{aligned} a^{\mathcal{E}}(\mathbf{u}, \mathbf{v}) &= j\omega\mu \int_S \bar{\mathbf{v}}(\mathbf{x}) \cdot \int_{S'} \mathbf{u}(\mathbf{x}') G(\mathbf{x}, \mathbf{x}') dS' dS - \frac{j}{\epsilon\omega} \int_S \nabla \cdot \bar{\mathbf{v}}(\mathbf{x}) \int_{S'} \nabla' \cdot \mathbf{u}(\mathbf{x}') G(\mathbf{x}, \mathbf{x}') dS' dS, \\ b^{\mathcal{E}}(\mathbf{u}, \mathbf{v}) &= \int_S \mathbf{u}(\mathbf{x}) \cdot \bar{\mathbf{v}}(\mathbf{x}) dS. \end{aligned}$$

Projecting (11) onto \mathbb{V} yields the variational form of the MFIE: find $\mathbf{J} \in \mathbb{V}$, such that

$$\frac{1}{2} \int_S \bar{\mathbf{v}} \cdot \mathbf{J} dS - \int_S \bar{\mathbf{v}}(\mathbf{x}) \cdot \left(\mathbf{n}(\mathbf{x}) \times \int_{S'} \mathbf{J}(\mathbf{x}') \times \nabla' G(\mathbf{x}, \mathbf{x}') dS' \right) dS = \int_S \bar{\mathbf{v}} \cdot (\mathbf{n} \times \mathbf{H}^{\mathcal{I}}) dS \quad (14)$$

for all $\mathbf{v} \in \mathbb{V}$. We can write (14) more succinctly as

$$a^{\mathcal{M}}(\mathbf{J}, \mathbf{v}) = b^{\mathcal{M}}(\mathbf{H}^{\mathcal{I}}, \mathbf{v}), \quad (15)$$

where the sesquilinear forms are defined by

$$\begin{aligned} a^{\mathcal{M}}(\mathbf{u}, \mathbf{v}) &= \frac{1}{2} \int_S \bar{\mathbf{v}}(\mathbf{x}) \cdot \mathbf{u}(\mathbf{x}) dS - \int_S \bar{\mathbf{v}}(\mathbf{x}) \cdot \left(\mathbf{n}(\mathbf{x}) \times \int_{S'} \mathbf{u}(\mathbf{x}') \times \nabla' G(\mathbf{x}, \mathbf{x}') dS' \right) dS, \\ b^{\mathcal{M}}(\mathbf{u}, \mathbf{v}) &= \int_S \bar{\mathbf{v}}(\mathbf{x}) \cdot [\mathbf{n}(\mathbf{x}) \times \mathbf{u}(\mathbf{x})] dS. \end{aligned}$$

The CFIE linearly combines the EFIE (13) and MFIE (15) to yield the variational problem: find $\mathbf{J} \in \mathbb{V}$, such that

$$a(\mathbf{J}, \mathbf{v}) = b(\mathbf{E}^{\mathcal{I}}, \mathbf{H}^{\mathcal{I}}, \mathbf{v}) \quad \forall \mathbf{v} \in \mathbb{V}, \quad (16)$$

where

$$a(\mathbf{J}, \mathbf{v}) = \frac{\alpha}{\eta} a^{\mathcal{E}}(\mathbf{J}, \mathbf{v}) + (1 - \alpha) a^{\mathcal{M}}(\mathbf{J}, \mathbf{v}), \quad (17)$$

$$b(\mathbf{E}^{\mathcal{I}}, \mathbf{H}^{\mathcal{I}}, \mathbf{v}) = \frac{\alpha}{\eta} b^{\mathcal{E}}(\mathbf{E}^{\mathcal{I}}, \mathbf{v}) + (1 - \alpha) b^{\mathcal{M}}(\mathbf{H}^{\mathcal{I}}, \mathbf{v}). \quad (18)$$

In (17) and (18), $\alpha \in [0, 1]$ is the combination parameter, and $\eta = \sqrt{\mu/\epsilon}$ is the characteristic impedance of the surrounding medium. It should be noted this is one of multiple choices for the CFIE [53, 54]; however, the verification methods presented in this paper can be applied to the other CFIE choices.

To solve the variational problem (16), we discretize S with a mesh composed of triangular elements and approximate \mathbf{J} with \mathbf{J}_h in terms of the Rao–Wilton–Glisson (RWG) basis functions $\mathbf{\Lambda}_j(\mathbf{x})$ [3]:

$$\mathbf{J}_h(\mathbf{x}) = \sum_{j=1}^{n_b} J_j \mathbf{\Lambda}_j(\mathbf{x}), \quad (19)$$

where n_b is the total number of basis functions. The RWG basis functions are second-order accurate [55, pp. 155–156], and are defined for a triangle pair by

$$\mathbf{\Lambda}_j(\mathbf{x}) = \begin{cases} \frac{\ell_j}{2A_j^+} \boldsymbol{\rho}_j^+, & \text{for } \mathbf{x} \in T_j^+ \\ \frac{\ell_j}{2A_j^-} \boldsymbol{\rho}_j^-, & \text{for } \mathbf{x} \in T_j^- \\ \mathbf{0}, & \text{otherwise} \end{cases},$$

where ℓ_j is the length of the edge shared by the triangle pair, and A_j^+ and A_j^- are the areas of the triangles T_j^+ and T_j^- associated with basis function j . $\boldsymbol{\rho}_j^+$ denotes the vector from the vertex of T_j^+ opposite the shared edge to \mathbf{x} , and $\boldsymbol{\rho}_j^-$ denotes the vector to the vertex of T_j^- opposite the shared edge from \mathbf{x} .

These basis functions ensure that \mathbf{J}_h is tangent to the mesh when using planar triangular elements. Additionally, along the shared edge of the triangle pair, the component of $\mathbf{\Lambda}_j(\mathbf{x})$ normal to that edge is unity. Therefore, for a triangle edge shared by only two triangles, the component of \mathbf{J}_h normal to that edge is J_j . The solution is considered most accurate at the midpoint of the edge [55, pp. 155–156]; therefore, we measure the solution at the midpoints.

Defining \mathbb{V}_h to be the span of RWG basis functions associated with the mesh on S , the Galerkin approximation of (16) is now: find $\mathbf{J}_h \in \mathbb{V}_h$, such that

$$a(\mathbf{J}_h, \boldsymbol{\Lambda}_i) = b(\mathbf{E}^{\mathcal{I}}, \mathbf{H}^{\mathcal{I}}, \boldsymbol{\Lambda}_i) \quad (20)$$

for $i = 1, \dots, n_b$. Letting \mathbf{J}^h denote the vector of coefficients used to construct \mathbf{J}_h (19), (20) can be written in matrix form as $\mathbf{Z}\mathbf{J}^h = \mathbf{V}$, where $Z_{i,j} = a(\boldsymbol{\Lambda}_j, \boldsymbol{\Lambda}_i)$ is the impedance matrix, $J_j^h = J_j$ is the current vector, and $V_i = b(\mathbf{E}^{\mathcal{I}}, \mathbf{H}^{\mathcal{I}}, \boldsymbol{\Lambda}_i)$ is the excitation vector.

3. Manufactured Solutions

We define the residual functional for each test basis function as

$$r_i(\mathbf{u}) = a(\mathbf{u}, \boldsymbol{\Lambda}_i) - b(\mathbf{E}^{\mathcal{I}}, \mathbf{H}^{\mathcal{I}}, \boldsymbol{\Lambda}_i). \quad (21)$$

We can write the variational form (16) in terms of (21) as

$$r_i(\mathbf{J}) = a(\mathbf{J}, \boldsymbol{\Lambda}_i) - b(\mathbf{E}^{\mathcal{I}}, \mathbf{H}^{\mathcal{I}}, \boldsymbol{\Lambda}_i) = 0. \quad (22)$$

Similarly, we can write the discretized problem (20) in terms of (21) as

$$r_i(\mathbf{J}_h) = a(\mathbf{J}_h, \boldsymbol{\Lambda}_i) - b(\mathbf{E}^{\mathcal{I}}, \mathbf{H}^{\mathcal{I}}, \boldsymbol{\Lambda}_i) = 0. \quad (23)$$

The method of manufactured solutions modifies (23) to be

$$r_i(\mathbf{J}_h) = r_i(\mathbf{J}_{\text{MS}}), \quad (24)$$

where \mathbf{J}_{MS} is the manufactured solution, and $\mathbf{r}(\mathbf{J}_{\text{MS}})$ is computed exactly.

Inserting (22) and (23) into (24) yields

$$a(\mathbf{J}_h, \boldsymbol{\Lambda}_i) = a(\mathbf{J}_{\text{MS}}, \boldsymbol{\Lambda}_i). \quad (25)$$

However, instead of solving (25), we can equivalently solve (20) by setting

$$b(\mathbf{E}^{\mathcal{I}}, \mathbf{H}^{\mathcal{I}}, \boldsymbol{\Lambda}_i) = a(\mathbf{J}_{\text{MS}}, \boldsymbol{\Lambda}_i). \quad (26)$$

Equation (26) is satisfied by [46]

$$\mathbf{E}^{\mathcal{I}} = \frac{j}{\epsilon\omega} \int_S [k^2 \mathbf{J}_{\text{MS}}(\mathbf{x}') G(\mathbf{x}, \mathbf{x}') + \nabla' \cdot \mathbf{J}_{\text{MS}}(\mathbf{x}') \nabla G(\mathbf{x}, \mathbf{x}')] dS',$$

which, from (9), is equivalent to

$$\mathbf{E}^{\mathcal{I}} = \frac{j}{\epsilon\omega} \int_{S'} [k^2 \mathbf{J}_{\text{MS}}(\mathbf{x}') G(\mathbf{x}, \mathbf{x}') - \nabla' \cdot \mathbf{J}_{\text{MS}}(\mathbf{x}') \nabla' G(\mathbf{x}, \mathbf{x}')] dS', \quad (27)$$

and [48]

$$\mathbf{H}^{\mathcal{I}} = \frac{1}{2} \mathbf{J}_{\text{MS}} \times \mathbf{n} - \int_{S'} \mathbf{J}_{\text{MS}}(\mathbf{x}') \times \nabla' G(\mathbf{x}, \mathbf{x}') dS'. \quad (28)$$

3.1. Solution-Discretization Error

In (20), if the integrals in $a(\cdot, \cdot)$ (17) and $b(\cdot, \cdot)$ (18) are evaluated exactly, the only contribution to the discretization error is the solution-discretization error. Solving for \mathbf{J}^h enables us to compute the discretization error

$$\mathbf{e}_{\mathbf{J}} = \mathbf{J}^h - \mathbf{J}_n, \quad (29)$$

where J_{n_j} denotes the component of \mathbf{J}_{MS} flowing from T_j^+ to T_j^- . The norm of (29) has the property $\|\mathbf{e}_{\mathbf{J}}\| \leq C_{\mathbf{J}} h^{p_{\mathbf{J}}}$, where $C_{\mathbf{J}}$ is a function of the solution derivatives, h is representative of the mesh size, and $p_{\mathbf{J}}$ is the order of accuracy. By performing a mesh-convergence study of the norm of the discretization error, we can ensure the expected order of accuracy is obtained. For the RWG basis functions, the expectation is second-order accuracy ($p_{\mathbf{J}} = 2$) when the error is evaluated at the edge centers [55].

3.2. Numerical-Integration Error

In practice, the integrals in $a(\cdot, \cdot)$ (17) and $b(\cdot, \cdot)$ (18) are evaluated numerically, yielding the approximations $a^q(\cdot, \cdot)$ and $b^q(\cdot, \cdot)$. $a^q(\cdot, \cdot)$ and $b^q(\cdot, \cdot)$ are obtained by integrating over each triangular element using quadrature, and generally incur a numerical-integration error. Therefore, it is important to measure the numerical-integration error without contamination from the solution-discretization error.

In [48], approaches are presented to isolate the numerical-integration error by canceling or eliminating the solution-discretization error. In this paper, we cancel the solution-discretization error and measure the numerical-integration error from

$$e_a(\mathbf{J}_{h_{\text{MS}}}) = a^q(\mathbf{J}_{h_{\text{MS}}}, \mathbf{J}_{h_{\text{MS}}}) - a(\mathbf{J}_{h_{\text{MS}}}, \mathbf{J}_{h_{\text{MS}}}), \quad (30)$$

$$e_b(\mathbf{J}_{h_{\text{MS}}}) = b^q(\mathbf{E}_{\text{MS}}^{\mathcal{I}}, \mathbf{H}_{\text{MS}}^{\mathcal{I}}, \mathbf{J}_{h_{\text{MS}}}) - b(\mathbf{E}_{\text{MS}}^{\mathcal{I}}, \mathbf{H}_{\text{MS}}^{\mathcal{I}}, \mathbf{J}_{h_{\text{MS}}}), \quad (31)$$

where $\mathbf{J}_{h_{\text{MS}}}$ is the basis-function representation of \mathbf{J}_{MS} , obtained from (19) by setting the coefficients J_j equal to the normal component of \mathbf{J}_{MS} at the midpoint of each edge associated with $\Lambda_j(\mathbf{x})$. The presence of the basis functions in the minuend and subtrahend of (30) and (31) cancels the solution-discretization error. Equations (30) and (31) have the properties $|e_a(\mathbf{J}_{h_{\text{MS}}})| \leq C_a h^{p_a}$ and $|e_b(\mathbf{J}_{h_{\text{MS}}})| \leq C_b h^{p_b}$, where C_a and C_b are functions of the integrand derivatives, and p_a and p_b depend on the quadrature accuracy.

Reference [48] shows that $e_a(\mathbf{J}_{h_{\text{MS}}})$ (30) and $e_b(\mathbf{J}_{h_{\text{MS}}})$ (31) are proportional to their influence on the discretization error $\mathbf{e}_{\mathbf{J}}$ (29).

4. Electromagnetic Integral Evaluations

As described in the introduction, integrals containing the Green's function (5) or its derivatives, such as those appearing in the manufactured electric field $\mathbf{E}^{\mathcal{I}}$ (27) and magnetic field $\mathbf{H}^{\mathcal{I}}$ (28) in $b(\mathbf{E}^{\mathcal{I}}, \mathbf{H}^{\mathcal{I}}, \Lambda_i)$ (20), are unable to be computed analytically. Additionally, the singularity when $R \rightarrow 0$ complicates their accurate approximation, potentially contaminating convergence studies.

In [46] and [48], this problem is mitigated by manufacturing the Green's function in terms of low, even powers of R , permitting the integrals in $a(\mathbf{J}_h, \Lambda_i)$ and $b(\mathbf{E}^{\mathcal{I}}, \mathbf{H}^{\mathcal{I}}, \Lambda_i)$ (20) to be computed analytically for many choices of \mathbf{J}_{MS} . The drawbacks of the manufactured Green's function are the lack of physical realism and the practically singular matrices arising from terms containing integrals of the Green's function or its derivatives. To mitigate the latter concern, an effective optimization approach was presented to provide a unique solution and detect coding errors.

In this paper, we optimally approximate the Green's function in terms of even powers of R . This enables us to compute the integrals in (20) exactly, while maintaining some of the physical realism of the actual Green's function. Additionally, the condition number of the impedance matrix remains low enough to conduct meaningful mesh-convergence studies.

4.1. Green's Function Approximation

We can write the Green's function (5) alternatively as $G(R) = G_r(R) + jG_i(R)$, where

$$G_r(R) = \frac{\cos(kR)}{4\pi R}, \quad G_i(R) = -\frac{\sin(kR)}{4\pi R}. \quad (32)$$

The Taylor series expansions of $G_r(R)$ and $G_i(R)$ (32) at $R = 0$ are

$$G_r(R) = \frac{1}{4\pi} \sum_{n=0}^{\infty} \frac{(-1)^n k^{2n}}{(2n)!} R^{2n-1}, \quad G_i(R) = -\frac{1}{4\pi} \sum_{n=0}^{\infty} \frac{(-1)^n k^{2n+1}}{(2n+1)!} R^{2n}. \quad (33)$$

As $R \rightarrow 0$, integrands with negative or odd powers of R , such as those appearing in $G_r(R)$ (33), are singular [15].

To avoid contamination from integrating singular integrands, we approximate $G(R)$ using even, nonnegative powers of R for $R \in [\delta, R_m]$, where $R_m = \max_{\mathbf{x}, \mathbf{x}' \in S} R$ is the maximum possible distance between two points on S and $\delta \rightarrow 0$. We introduce the inner product

$$\langle u, v \rangle = \int_{\delta}^{R_m} u(R) \bar{v}(R) R dR, \quad (34)$$

with the norm $\|\cdot\|_R = \langle \cdot, \cdot \rangle^{1/2}$. Let $\phi_n(R)$ denote the orthonormal basis arising from the functions R^{2n} for $n \in \mathbb{N}_0$, subject to (34). $G(R)$ is approximated by

$$G(R) \approx \tilde{G}(R) = \sum_{n=0}^{n_m} G_n \phi_n(R), \quad (35)$$

where n_m denotes the truncation of an infinite series, and the coefficients G_n are obtained by minimizing $e_G^2 = \|\tilde{G} - G\|_R^2 = \|\tilde{G}_r - G_r\|_R^2 + \|\tilde{G}_i - G_i\|_R^2$. By setting $\partial e_G / \partial G_n = 0$, $G_n = \langle G, \phi_n \rangle$.

For G_i , $\|\tilde{G}_i - G_i\|_R^2$ and G_{i_n} are bounded for $\delta = 0$ in (34). For G_r , $\|\tilde{G}_r - G_r\|_R^2$ is bounded for $\delta > 0$ but not for $\delta = 0$. However, G_{r_n} is bounded for $\delta \geq 0$. Therefore, we compute the approximation (35) for $\delta = 0$ in (34).

Figure 1 shows \tilde{G} for multiple choices of k and n_m . For G_r , increasing n_m improves the approximation \tilde{G}_r but introduces spurious oscillations that require finer discretizations for mesh-convergence studies. Therefore, we approximate the Green's function with only the imaginary contribution by setting $G_{r_n} = 0$.

4.2. Incident Field Integral Evaluations

In $b(\mathbf{E}^{\mathcal{I}}, \mathbf{H}^{\mathcal{I}}, \mathbf{A}_i)$ (20), $\mathbf{E}^{\mathcal{I}}$ (27) and $\mathbf{H}^{\mathcal{I}}$ (28) take the form

$$\mathbf{E}^{\mathcal{I}} = \frac{j}{\epsilon\omega} (k^2 \mathbf{I}_{\mathcal{E}_A} - \mathbf{I}_{\mathcal{E}_\Phi}), \quad (36)$$

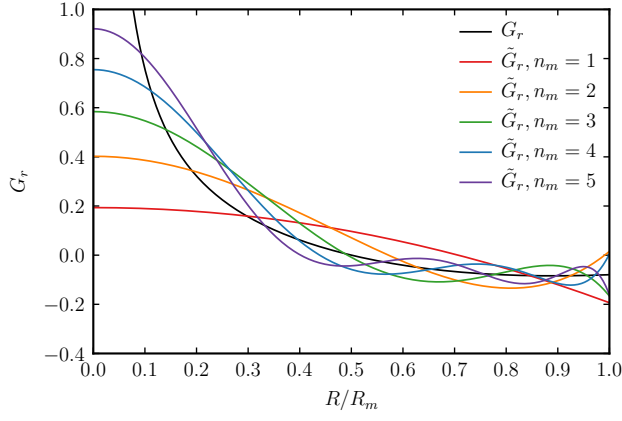
$$\mathbf{H}^{\mathcal{I}} = \frac{1}{2} \mathbf{J}_{\text{MS}} \times \mathbf{n} - \mathbf{I}_{\mathcal{M}}, \quad (37)$$

where

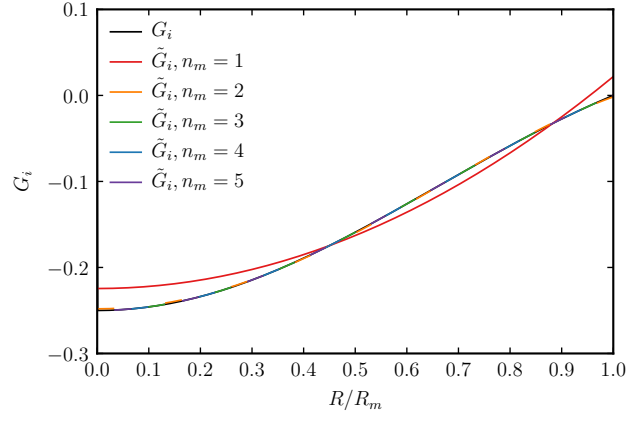
$$\mathbf{I}_{\mathcal{E}_A}(\mathbf{x}) = \int_{S'} \mathbf{J}_{\text{MS}}(\mathbf{x}') G(\mathbf{x}, \mathbf{x}') dS', \quad (38)$$

$$\mathbf{I}_{\mathcal{E}_\Phi}(\mathbf{x}) = \int_{S'} \nabla' \cdot \mathbf{J}_{\text{MS}}(\mathbf{x}') \nabla' G(\mathbf{x}, \mathbf{x}') dS', \quad (39)$$

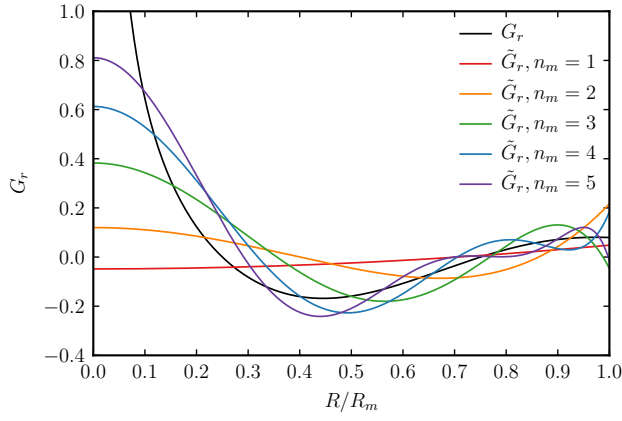
$$\mathbf{I}_{\mathcal{M}}(\mathbf{x}) = \int_{S'} \mathbf{J}_{\text{MS}}(\mathbf{x}') \times \nabla' G(\mathbf{x}, \mathbf{x}') dS' \quad (40)$$



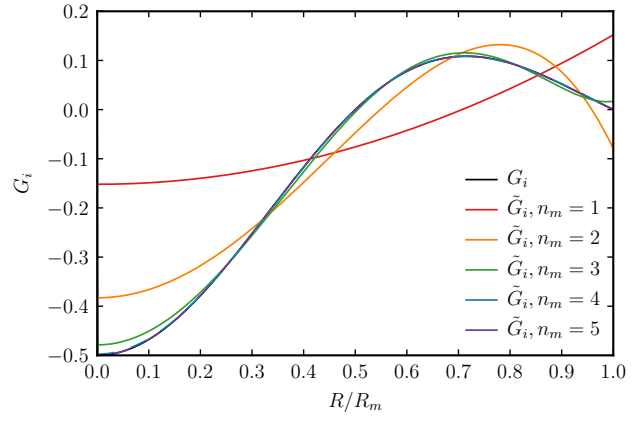
(a) $G_r, k = \pi/L$



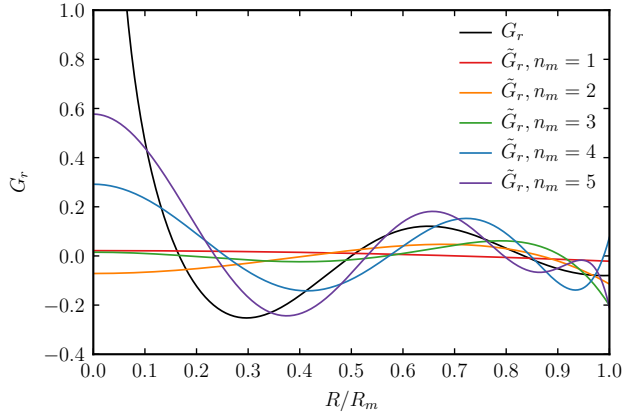
(b) $G_i, k = \pi/L$



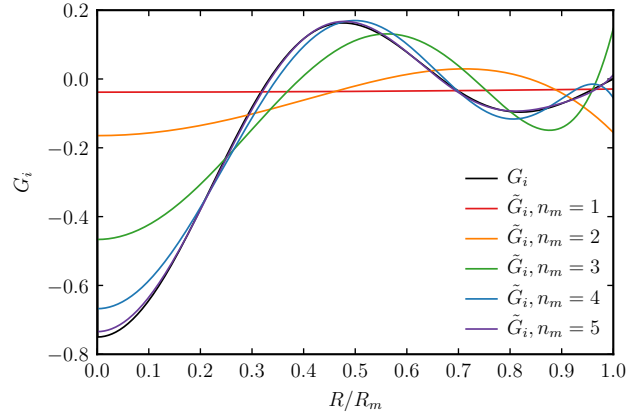
(c) $G_r, k = 2\pi/L$



(d) $G_i, k = 2\pi/L$



(e) $G_r, k = 3\pi/L$



(f) $G_i, k = 3\pi/L$

Figure 1: Approximations $\tilde{G} = \tilde{G}_r + j\tilde{G}_i$ for $G = G_r + jG_i$ ($L = R_m = 1$ m).

are the integrals that contain the Green's function. To evaluate these integrals, we replace G with \tilde{G} (35), which can be written alternatively as

$$\tilde{G}(R) = \sum_{n=0}^{n_m} \tilde{G}_n R^{2n}, \quad (41)$$

such that

$$\nabla' \tilde{G}(R) = -\frac{\tilde{G}'(R)}{R} \mathbf{R} = -2\mathbf{R} \sum_{n=1}^{n_m} n \tilde{G}_n R^{2(n-1)}. \quad (42)$$

Inserting (41) into (38) and inserting (42) into (39) and (40), (38)–(40) become

$$\mathbf{I}_{\mathcal{E}_A}(\mathbf{x}) = \sum_{n=0}^{n_m} \tilde{G}_n \int_{S'} R^{2n} \mathbf{J}_{\text{MS}}(\mathbf{x}') dS', \quad (43)$$

$$\mathbf{I}_{\mathcal{E}_\Phi}(\mathbf{x}) = -2 \sum_{n=1}^{n_m} n \tilde{G}_n \int_{S'} R^{2(n-1)} \nabla' \cdot \mathbf{J}_{\text{MS}}(\mathbf{x}') \mathbf{R} dS', \quad (44)$$

$$\mathbf{I}_{\mathcal{M}}(\mathbf{x}) = -2 \sum_{n=1}^{n_m} n \tilde{G}_n \int_{S'} R^{2(n-1)} \mathbf{J}_{\text{MS}}(\mathbf{x}') \times \mathbf{R} dS'. \quad (45)$$

The evaluation of (43)–(45) is discussed in Appendix A for the cases presented in Section 5.

5. Numerical Examples

In this section, we demonstrate the approaches described in Section 3 by isolating and measuring the solution-discretization error (Section 3.1) and the numerical-integration error (Section 3.2). We consider two domains: a cube and an equilateral triangular prism, each with all edges of length $L = 1$ m. These domains are shown in Figures 2 and 3 with the total number of triangles $n_t = 1200$ for the cube and $n_t = 800$ for the triangular prism.

For both domains, we introduce a coordinate system $\boldsymbol{\xi}$ that is fixed to the n_s surfaces for which $\mathbf{n} \cdot \mathbf{e}_y = 0$. For the cube, $\xi \in [0, 4L]$ is perpendicular to y , wrapping around the surfaces for which $\mathbf{n} \cdot \mathbf{e}_y = 0$, beginning at $x = 0$ and $z = L$. For the triangular prism, $\xi \in [0, 3L]$ is perpendicular to y , wrapping around the surfaces for which $\mathbf{n} \cdot \mathbf{e}_y = 0$, beginning at $x = z = 0$. For both cases, $\eta \in [0, L]$ is equal to y . $\boldsymbol{\xi}$ is depicted in Figure 3, which shows the nets of these domains. The transformation between $\boldsymbol{\xi}$ and \mathbf{x} for the two domains, which is defined in a piecewise manner for each of the n_s surfaces, is listed in Table 1. Table 1 additionally lists the ξ domain $[\xi_{a_j}, \xi_{b_j}]$ for each of the n_s surfaces.

We manufacture the surface current density $\mathbf{J}_{\text{MS}}(\mathbf{x}) = J_\xi(\boldsymbol{\xi}) \mathbf{e}_\xi$, where

$$J_\xi(\boldsymbol{\xi}) = J_0 \begin{cases} \sin(\beta\xi/L) \sin^3(\pi\eta/L), & \text{for } \mathbf{n} \cdot \mathbf{e}_y = 0 \\ 0, & \text{for } \mathbf{n} \cdot \mathbf{e}_y \neq 0 \end{cases}, \quad (46)$$

$J_0 = 1$ A/m, and $\beta = \pi/2$ for the cube and $\beta = 2\pi/3$ for the triangular prism. In the \mathbf{x} -coordinate system, $\mathbf{e}_\xi = (\partial\mathbf{x}/\partial\xi)_j$. Equation (46) is chosen because it is of class C^2 and its oscillations are minimal, such that finer meshes are not required for mesh-convergence studies. Figures 4 and 5 show plots of (46). Additionally we set the permeability and permittivity of the surrounding medium to those of free space: $\mu = 1.25663706212 \times 10^{-6}$ N/A² and $\epsilon = 8.8541878128 \times 10^{-12}$ F/m.

When solving (20), numerical integration is performed using polynomial quadrature rules for triangles. For multiple quadrature point amounts, Table 2 lists the maximum polynomial degree of the integrand the points can integrate exactly [56, 57], as well as the convergence rates of the errors for inexact integrations of nonsingular integrands. These properties correspond to the optimal point locations and weights. Figure 6a shows the optimal 6-point quadrature rule, which can exactly integrate polynomials up to degree 4.

To evaluate $b(\mathbf{E}^{\mathcal{I}}, \mathbf{H}^{\mathcal{I}}, \boldsymbol{\Lambda}_j)$ in (20), we use \tilde{G} (35) to compute the integrals $\mathbf{I}_{\mathcal{E}_A}$ (38), $\mathbf{I}_{\mathcal{E}_\Phi}$ (39), and $\mathbf{I}_{\mathcal{M}}$ (40) in $\mathbf{E}^{\mathcal{I}}$ (36) and $\mathbf{H}^{\mathcal{I}}$ (37) analytically, as shown in Appendix A. Setting $n_m = 5$, $\mathbf{I}_{\mathcal{E}_A}$, $\mathbf{I}_{\mathcal{E}_\Phi}$, and

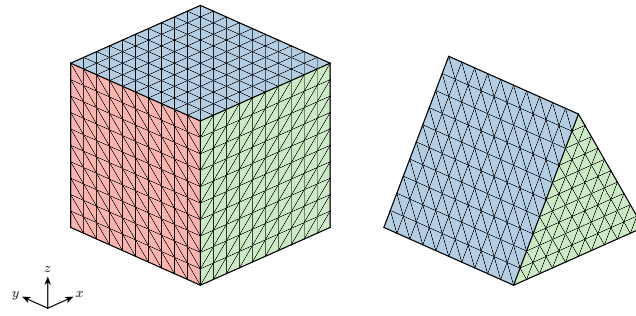


Figure 2: Dimetric view of meshes for the cube with $n_t = 1200$ (left) and triangular prism with $n_t = 800$ (right).

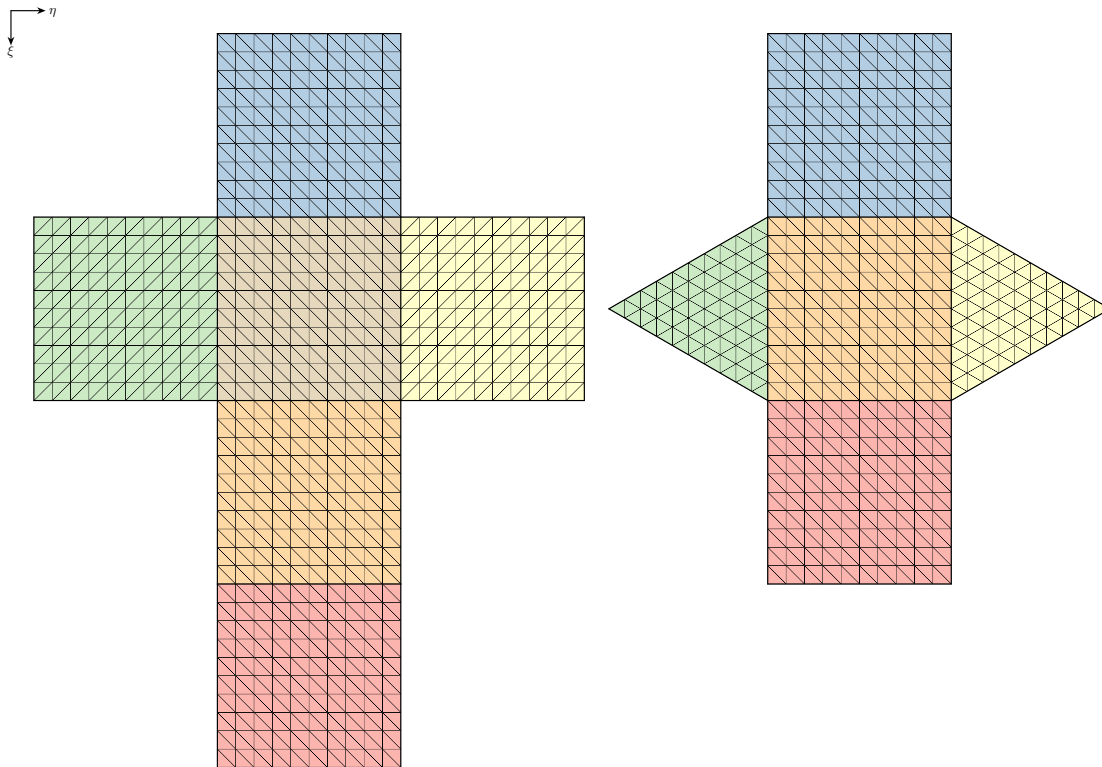


Figure 3: Net view of meshes for the cube with $n_t = 1200$ (left) and the triangular prism with $n_t = 800$ (right).

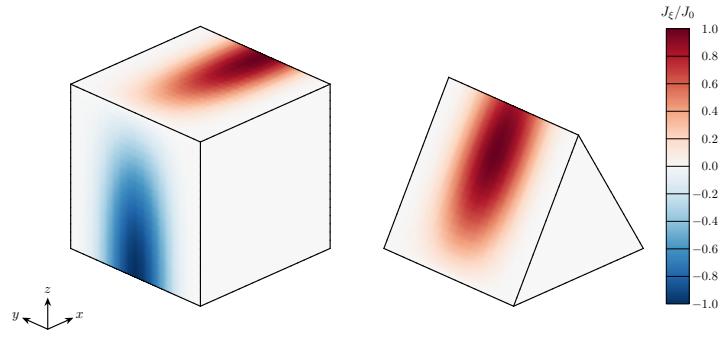


Figure 4: Dimetric view of manufactured surface current density \mathbf{J}_{MS} for the cube (left) and triangular prism (right).

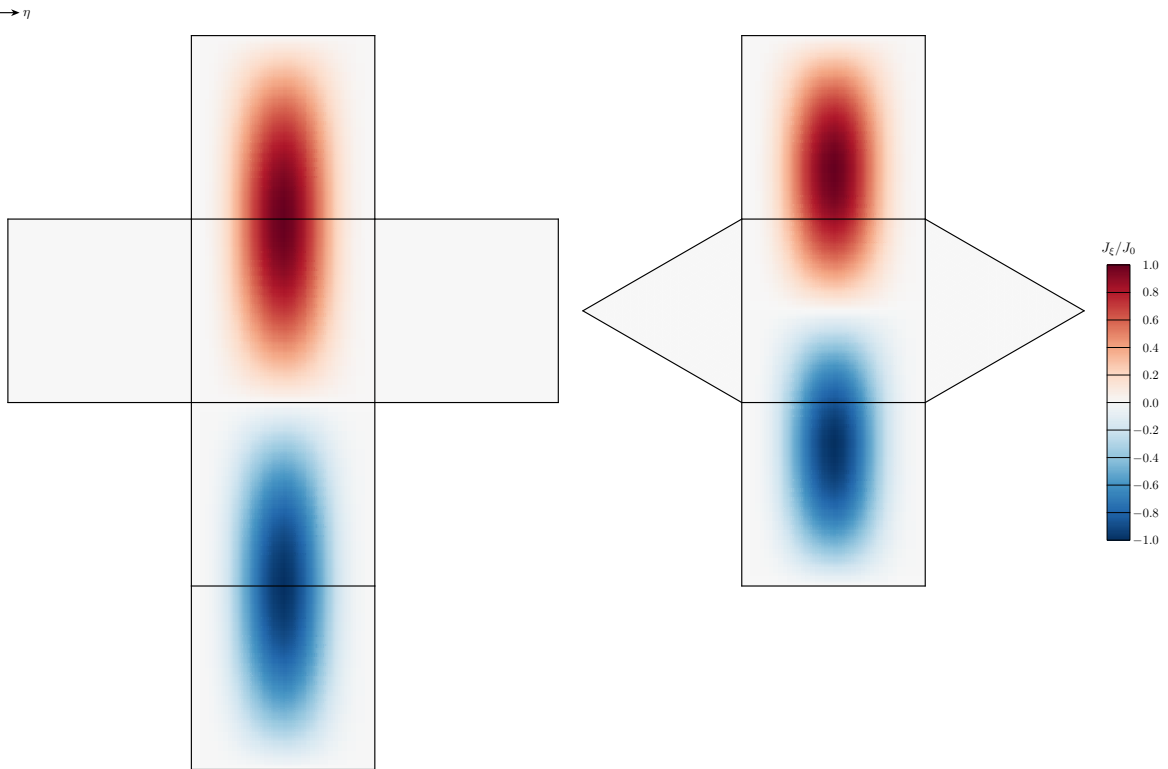


Figure 5: Net view of manufactured surface current density \mathbf{J}_{MS} for the cube (left) and triangular prism (right).

j	$[\xi_{a_j}, \xi_{b_j}]$	Cube			Triangular Prism		
		$\mathbf{x}_j(\boldsymbol{\xi})$	$\left(\frac{\partial \mathbf{x}}{\partial \boldsymbol{\xi}}\right)_j$		$\mathbf{x}_j(\boldsymbol{\xi})$	$\left(\frac{\partial \mathbf{x}}{\partial \boldsymbol{\xi}}\right)_j$	
1	$[0, 1]L$	$\left(\frac{\partial \mathbf{x}}{\partial \boldsymbol{\xi}}\right)_j \boldsymbol{\xi} + \begin{Bmatrix} 0 \\ 0 \\ 1 \end{Bmatrix} L$	$\begin{bmatrix} 1 & 0 & 0 \\ 0 & 1 & 0 \\ 0 & 0 & 1 \end{bmatrix}$	$\left(\frac{\partial \mathbf{x}}{\partial \boldsymbol{\xi}}\right)_j \boldsymbol{\xi} + \begin{Bmatrix} 0 \\ 0 \\ 0 \end{Bmatrix} L$	$\begin{bmatrix} 1/2 & 0 & -\sqrt{3}/2 \\ 0 & 1 & 0 \\ \sqrt{3}/2 & 0 & 1/2 \end{bmatrix}$		
2	$[1, 2]L$	$\left(\frac{\partial \mathbf{x}}{\partial \boldsymbol{\xi}}\right)_j \boldsymbol{\xi} + \begin{Bmatrix} 1 \\ 0 \\ 2 \end{Bmatrix} L$	$\begin{bmatrix} 0 & 0 & 1 \\ 0 & 1 & 0 \\ -1 & 0 & 0 \end{bmatrix}$	$\left(\frac{\partial \mathbf{x}}{\partial \boldsymbol{\xi}}\right)_j \boldsymbol{\xi} + \begin{Bmatrix} 0 \\ 0 \\ \sqrt{3} \end{Bmatrix} L$	$\begin{bmatrix} 1/2 & 0 & \sqrt{3}/2 \\ 0 & 1 & 0 \\ -\sqrt{3}/2 & 0 & 1/2 \end{bmatrix}$		
3	$[2, 3]L$	$\left(\frac{\partial \mathbf{x}}{\partial \boldsymbol{\xi}}\right)_j \boldsymbol{\xi} + \begin{Bmatrix} 3 \\ 0 \\ 0 \end{Bmatrix} L$	$\begin{bmatrix} -1 & 0 & 0 \\ 0 & 1 & 0 \\ 0 & 0 & -1 \end{bmatrix}$	$\left(\frac{\partial \mathbf{x}}{\partial \boldsymbol{\xi}}\right)_j \boldsymbol{\xi} + \begin{Bmatrix} 3 \\ 0 \\ 0 \end{Bmatrix} L$	$\begin{bmatrix} -1 & 0 & 0 \\ 0 & 1 & 0 \\ 0 & 0 & -1 \end{bmatrix}$		
4	$[3, 4]L$	$\left(\frac{\partial \mathbf{x}}{\partial \boldsymbol{\xi}}\right)_j \boldsymbol{\xi} + \begin{Bmatrix} 0 \\ 0 \\ -3 \end{Bmatrix} L$	$\begin{bmatrix} 0 & 0 & -1 \\ 0 & 1 & 0 \\ 1 & 0 & 0 \end{bmatrix}$				

Table 1: Transformations between $\boldsymbol{\xi}$ and \mathbf{x} for the cube and triangular prism.

Maximum integrand degree	Number of points	Convergence rate	Maximum integrand degree	Number of points	Convergence rate
1	1	$\mathcal{O}(h^2)$	7	13	$\mathcal{O}(h^8)$
2	3	$\mathcal{O}(h^4)$	8	16	$\mathcal{O}(h^{10})$
3	4	$\mathcal{O}(h^4)$	9	19	$\mathcal{O}(h^{10})$
4	6	$\mathcal{O}(h^6)$	10	25	$\mathcal{O}(h^{12})$
5	7	$\mathcal{O}(h^6)$	11	27	$\mathcal{O}(h^{12})$
6	12	$\mathcal{O}(h^8)$	12	33	$\mathcal{O}(h^{14})$

Table 2: Polynomial triangle quadrature properties.

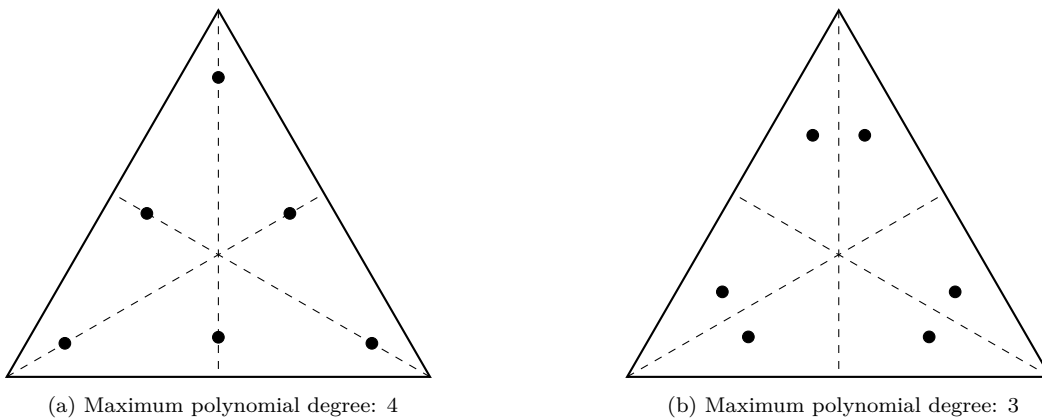


Figure 6: 6-point quadrature rules.

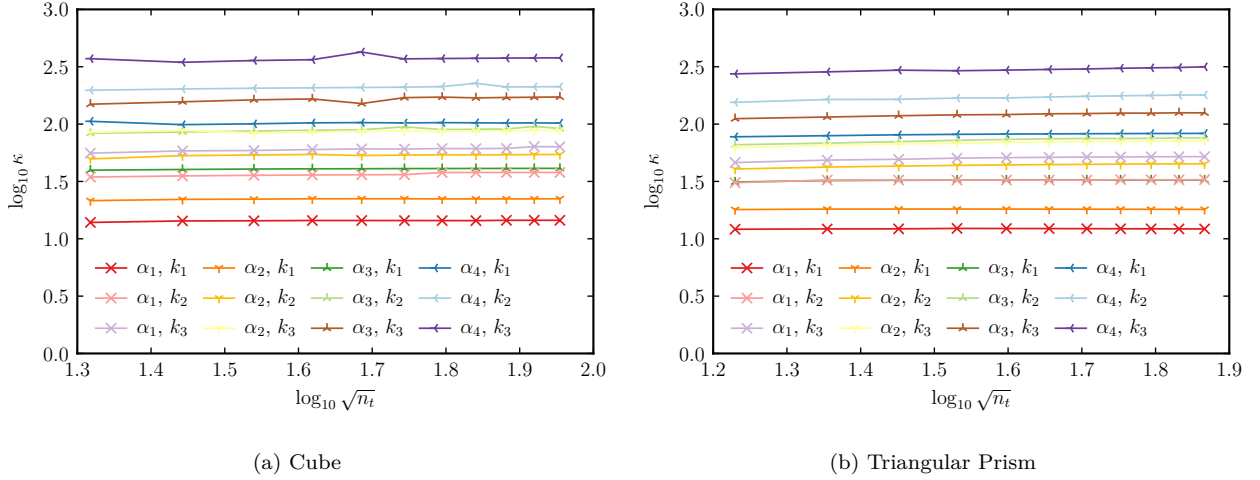


Figure 7: Solution-discretization error: Condition numbers of the impedance matrix \mathbf{Z} for $\alpha_m = m/5$, $k_n = n\pi/L$.

$\mathbf{I}_{\mathcal{M}}$ yield polynomials in \mathbf{x} of degrees 10, 9, and 9, respectively. In $b(\mathbf{E}^{\mathcal{I}}, \mathbf{H}^{\mathcal{I}}, \mathbf{\Lambda}_i)$, multiplication with $\mathbf{\Lambda}_i$ increases these degrees by a power. Therefore, a 27-point polynomial quadrature rule, which can exactly evaluate integrals up to degree 11, can be used to evaluate the integrals.

To evaluate $a(\mathbf{J}_h, \mathbf{\Lambda}_i)$ in (20), we note that \tilde{G} (35) is a polynomial in \mathbf{x} and \mathbf{x}' of degree 10, and $\nabla' \tilde{G}$ is a polynomial in \mathbf{x} and \mathbf{x}' of degree 9. In $a(\mathbf{J}_h, \mathbf{\Lambda}_i)$, multiplication with $\mathbf{\Lambda}_i(\mathbf{x})$ and $\mathbf{\Lambda}_j(\mathbf{x}')$ increases these degrees by a power, such that a 27-point polynomial quadrature rule can be used to evaluate the integrals with respect to \mathbf{x} and \mathbf{x}' .

5.1. Solution-Discretization Error

To isolate and measure the solution-discretization error, we proceed with the assessment described in Section 3.1. As stated previously, integrals on both sides of (20) are computed exactly with a 27-point polynomial quadrature rule.

To account for potential disparities in the magnitudes of the terms, we consider four values of α : $\alpha_m = m/5$, for $m = 1, \dots, 4$, and three values of k : $k_n = n\pi/L$, for $n = 1, \dots, 3$. For both domains, Figure 7 shows how the condition numbers κ of the impedance matrix \mathbf{Z} from these 12 combinations vary with respect to mesh size. The condition numbers are low enough to conduct meaningful convergence studies.

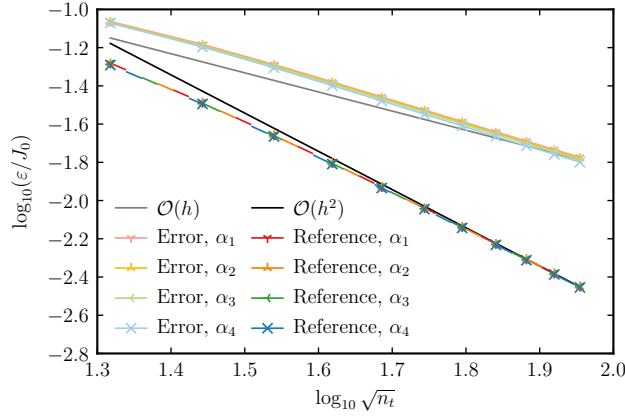
Figure 8 shows the L^∞ -norm of the discretization error $\|\mathbf{e}_{\mathbf{J}}\|_\infty$ (29) arising from only the solution-discretization error for both domains. The convergence rates for these cases, which are denoted as reference cases, are all $\mathcal{O}(h^2)$ as expected.

To test the ability to detect a coding error, we multiply the diagonal elements of the impedance matrix by $(1 + n_t^{-1/2})$. In Figure 8, these cases with the coding error are $\mathcal{O}(h)$, instead of $\mathcal{O}(h^2)$. Therefore, the coding error is detected.

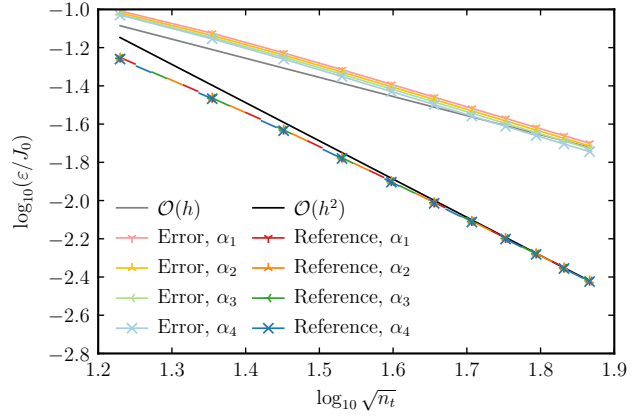
5.2. Numerical-Integration Error

To isolate and measure the numerical-integration error, we perform the assessments described in Section 3.2.

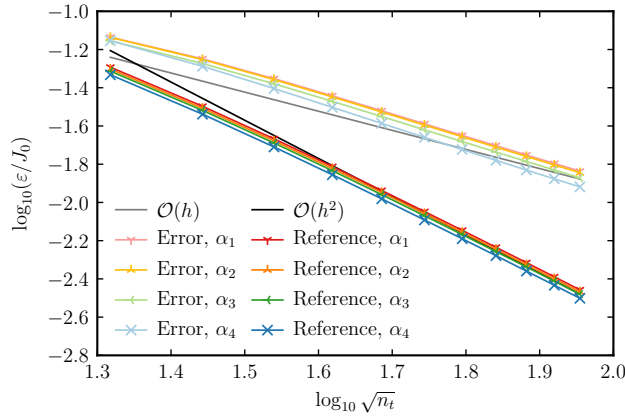
For both domains and the most extreme combinations of α and k , Figures 9 and 10 show the numerical-integration error $e_a(\mathbf{J}_{h_{\text{MS}}})$ (30) when the solution-discretization error is canceled. In the legend entries, the first number is the amount of quadrature points used to compute the integral over S , whereas the second is the amount used to compute the integral over S' . The numerical-integration error is nondimensionalized by the constant $\varepsilon_0 = 1 \text{ A}^2$. Each of the solutions converges at the expected rate listed in Table 2. For the finest meshes considered, the round-off error arising from the double-precision calculations exceeds the numerical-integration error.



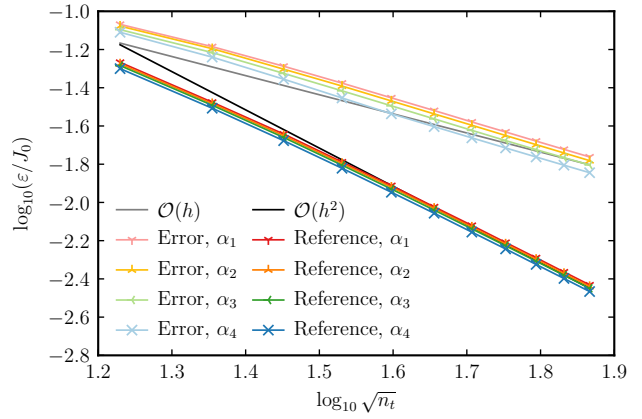
(a) Cube, $\alpha_m = m/5, k = \pi/L$



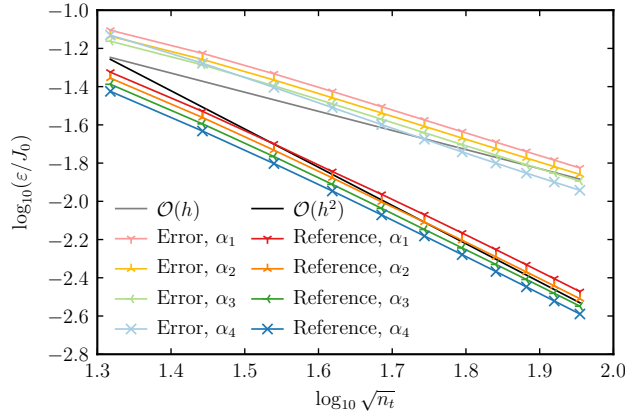
(b) Triangular Prism, $\alpha_m = m/5, k = \pi/L$



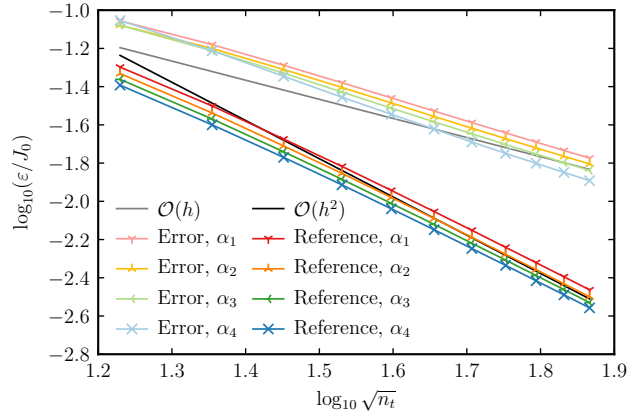
(c) Cube, $\alpha_m = m/5, k = 2\pi/L$



(d) Triangular Prism, $\alpha_m = m/5, k = 2\pi/L$

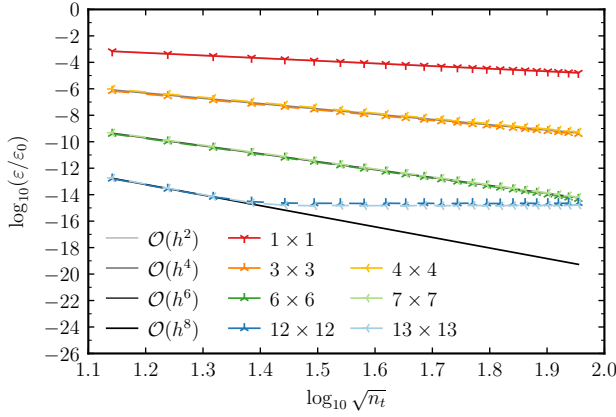


(e) Cube, $\alpha_m = m/5, k = 3\pi/L$

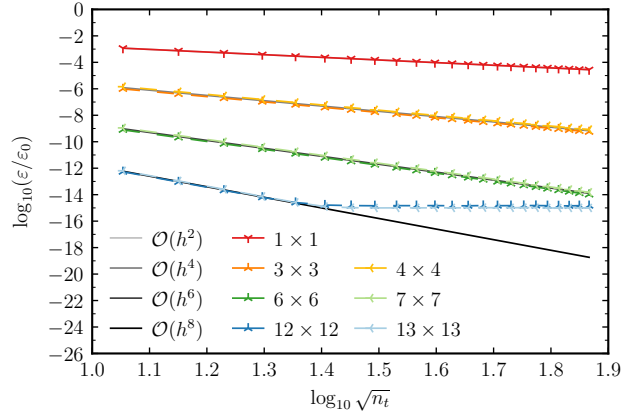


(f) Triangular Prism, $\alpha_m = m/5, k = 3\pi/L$

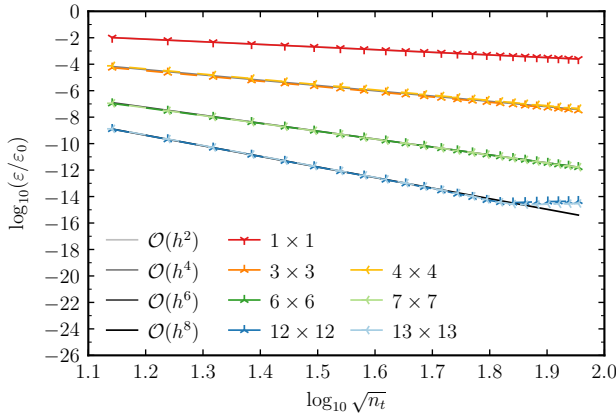
Figure 8: Solution-discretization error: $\varepsilon = \|\mathbf{e}_J\|_\infty$.



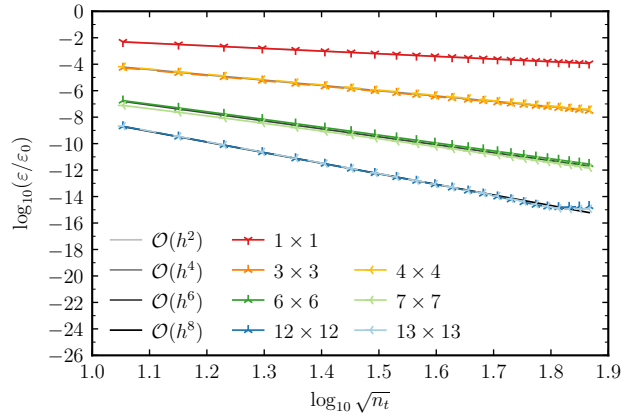
(a) Cube, $\alpha = 1/5$, $k = \pi/L$



(b) Triangular Prism, $\alpha = 1/5$, $k = \pi/L$



(c) Cube, $\alpha = 1/5$, $k = 3\pi/L$



(d) Triangular Prism, $\alpha = 1/5$, $k = 3\pi/L$

Figure 9: Numerical-integration error: $\varepsilon = |e_a(\mathbf{J}_{h_{MS}})|$ (30) for different amounts of quadrature points.

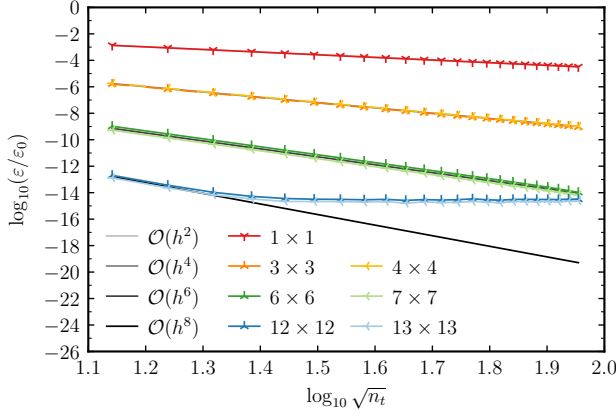
To test the ability to detect a coding error, we replace the optimal 6-point quadrature rule that can exactly integrate polynomials up to degree 4 (Figure 6a) with a suboptimal rule [58] (Figure 6b) that can integrate polynomials up to degree 3. Figure 11 shows how the cases with this coding error compare with the cases presented in Figures 9 and 10. In Figure 11, the convergence rates are $\mathcal{O}(h^4)$ for the cases with the coding error, compared to the expected $\mathcal{O}(h^6)$ rates without. Therefore, $e_a(\mathbf{J}_{h_{MS}})$ detects the coding error.

Figures 12 and 13 show the numerical-integration error $e_b(\mathbf{J}_{h_{MS}})$ (31) when the solution-discretization error is canceled. In the legend entries, the number is the amount of quadrature points used to compute the integral. Each of the solutions converges at the expected rate. For the finest meshes considered, the round-off error arising from the double-precision calculations exceeds the numerical-integration error.

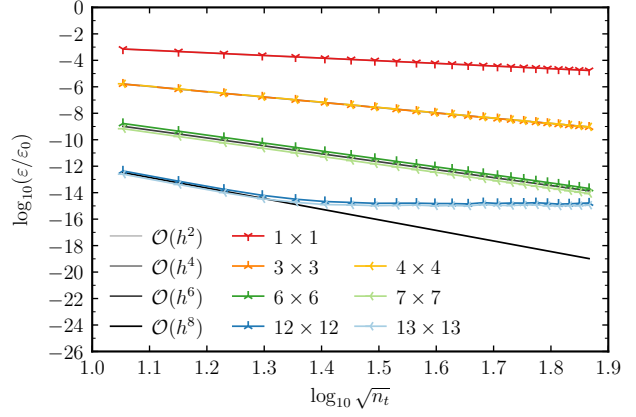
Figure 14 shows how the cases with this coding error compare with the cases presented in Figures 12 and 13. In Figure 14, the convergence rates are $\mathcal{O}(h^4)$ for the cases with the coding error, compared to the expected $\mathcal{O}(h^6)$ rates without. Therefore, $e_b(\mathbf{J}_{h_{MS}})$ detects the coding error.

6. Conclusions

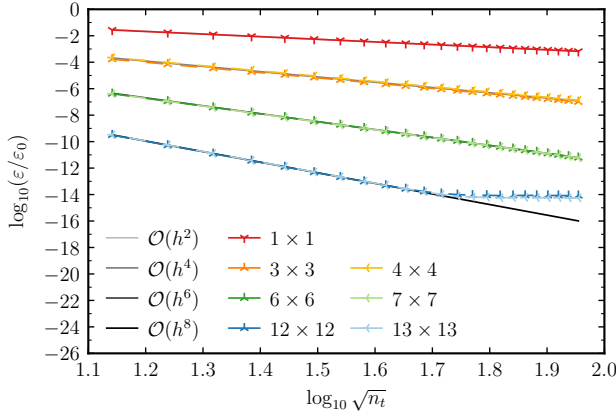
In this paper, we presented code-verification approaches for the method-of-moments implementation of the combined-field integral equation to isolate and measure the solution-discretization error and numerical-integration error. To isolate the solution-discretization error, we approximated the Green's function using a



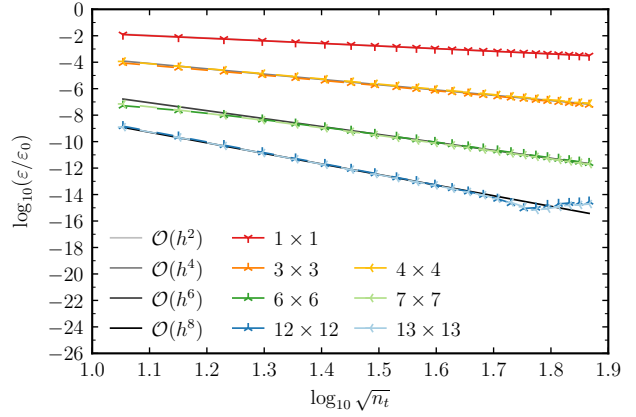
(a) Cube, $\alpha = 4/5$, $k = \pi/L$



(b) Triangular Prism, $\alpha = 4/5$, $k = \pi/L$

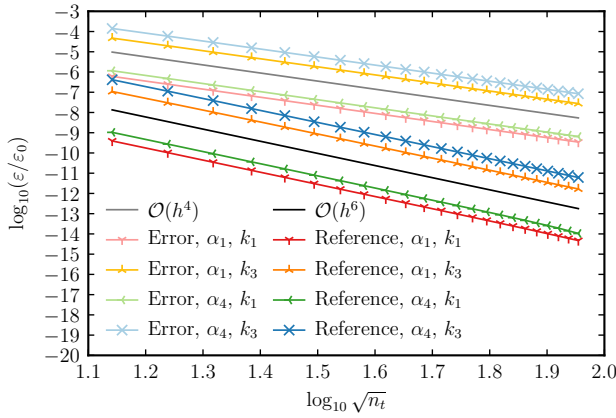


(c) Cube, $\alpha = 4/5$, $k = 3\pi/L$

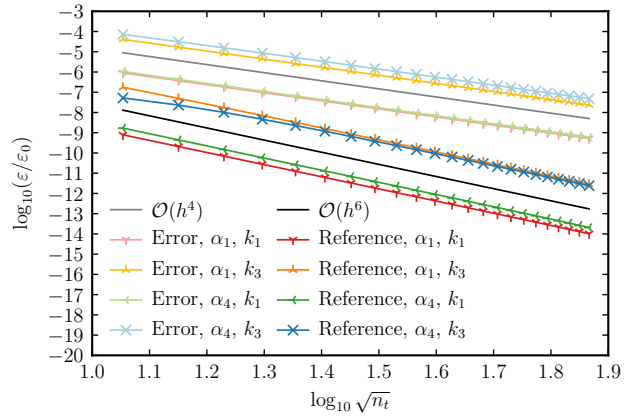


(d) Triangular Prism, $\alpha = 4/5$, $k = 3\pi/L$

Figure 10: Numerical-integration error: $\varepsilon = |e_a(\mathbf{J}_{h_{MS}})|$ (30) for different amounts of quadrature points.

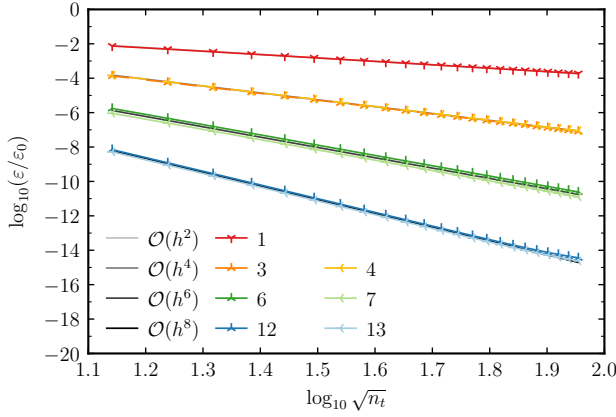


(a) Cube, $\alpha_m = m/5$, $k_n = n\pi/L$

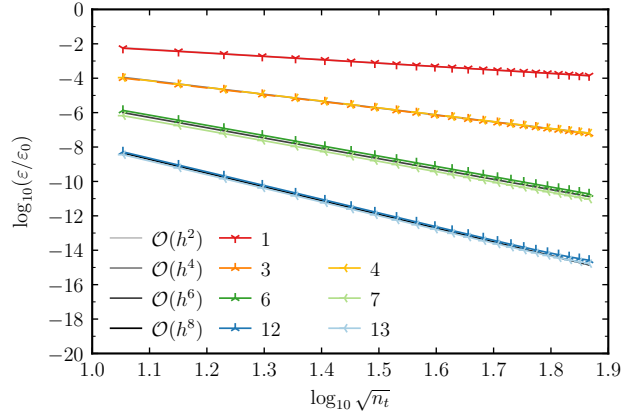


(b) Triangular Prism, $\alpha_m = m/5$, $k_n = n\pi/L$

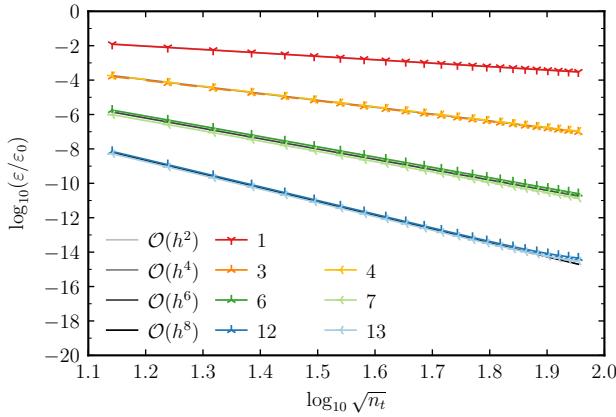
Figure 11: Numerical-integration error: $\varepsilon = |e_a(\mathbf{J}_{h_{MS}})|$ (30) in the presence of a coding error.



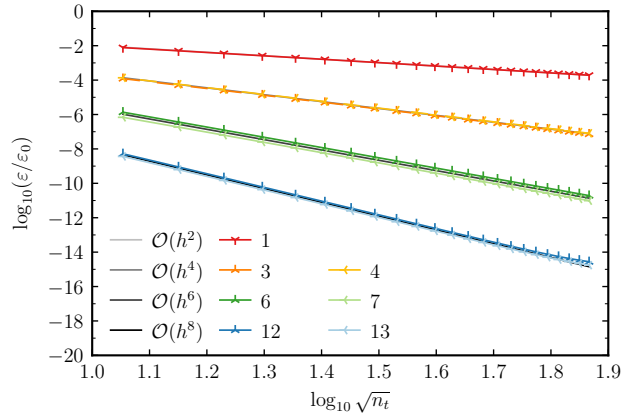
(a) Cube, $\alpha = 1/5$, $k = \pi/L$



(b) Triangular Prism, $\alpha = 1/5$, $k = \pi/L$



(c) Cube, $\alpha = 1/5$, $k = 3\pi/L$



(d) Triangular Prism, $\alpha = 1/5$, $k = 3\pi/L$

Figure 12: Numerical-integration error: $\varepsilon = |e_b(\mathbf{J}_{h_{\text{MS}}})|$ (31) for different amounts of quadrature points.

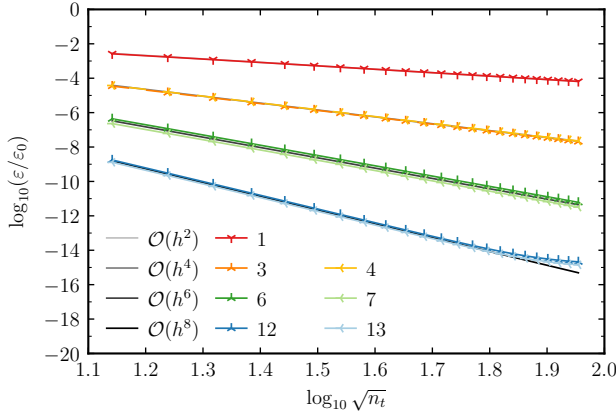
basis that can be integrated exactly, eliminating the numerical-integration error. To isolate the numerical-integration error, we removed the solution-discretization error by canceling the basis-function contribution.

For both approaches, we considered different wavenumbers and combination parameters to vary the relative weights between the terms in the combined-field integral equation. For these different cases, we achieved the expected orders of accuracy for cases without coding errors, and we were able to detect cases with coding errors.

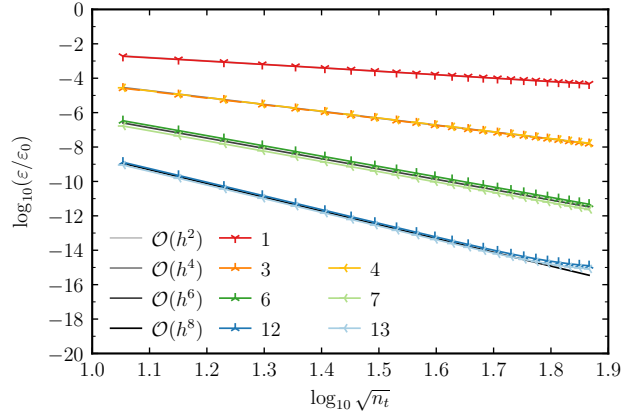
This work can be complemented with unit tests that assess the evaluation of the (nearly) singular integrals that arise from the actual Green's function.

Acknowledgments

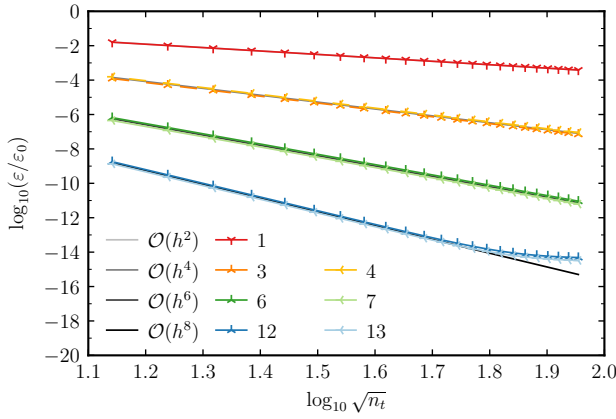
The authors thank Timothy Smith for his insightful feedback. This article has been authored by employees of National Technology & Engineering Solutions of Sandia, LLC under Contract No. DE-NA0003525 with the U.S. Department of Energy (DOE). The employees own all right, title, and interest in and to the article and are solely responsible for its contents. The United States Government retains and the publisher, by accepting the article for publication, acknowledges that the United States Government retains a non-exclusive, paid-up, irrevocable, world-wide license to publish or reproduce the published form of this article or allow others to do so, for United States Government purposes. The DOE will provide public access



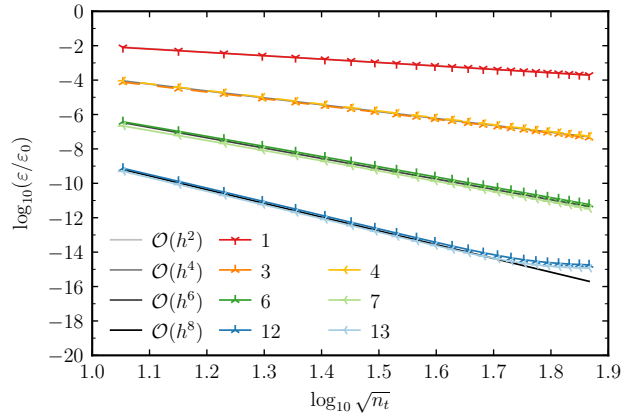
(a) Cube, $\alpha = 4/5$, $k = \pi/L$



(b) Triangular Prism, $\alpha = 4/5$, $k = \pi/L$

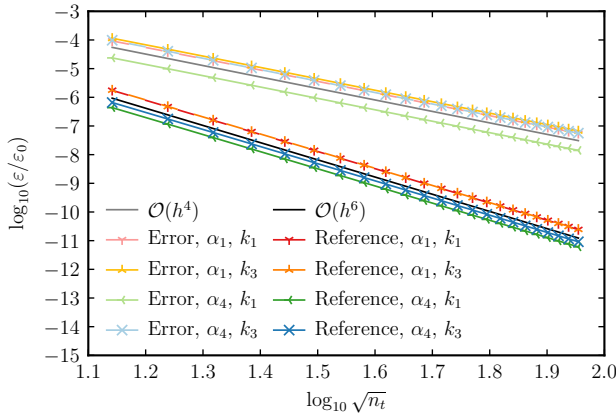


(c) Cube, $\alpha = 4/5$, $k = 3\pi/L$

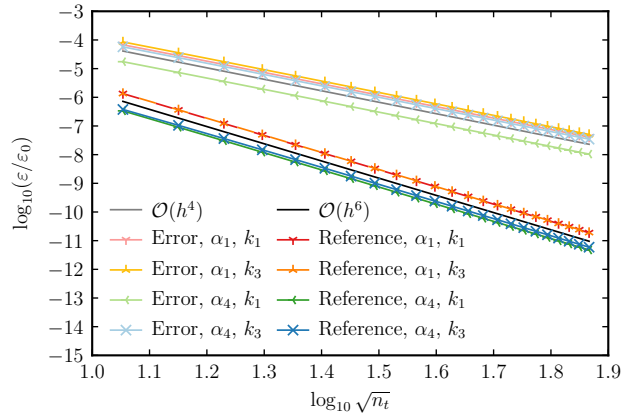


(d) Triangular Prism, $\alpha = 4/5$, $k = 3\pi/L$

Figure 13: Numerical-integration error: $\varepsilon = |e_b(\mathbf{J}_{h_{MS}})|$ (31) for different amounts of quadrature points.



(a) Cube, $\alpha_m = m/5$, $k_n = n\pi/L$



(b) Triangular Prism, $\alpha_m = m/5$, $k_n = n\pi/L$

Figure 14: Numerical-integration error: $\varepsilon = |e_b(\mathbf{J}_{h_{MS}})|$ (31) in the presence of a coding error.

to these results of federally sponsored research in accordance with the DOE Public Access Plan <https://www.energy.gov/downloads/doe-public-access-plan>.

Appendix A. Incident Field Integral Evaluations for Section 5

The integration with respect to \mathbf{x}' in $\mathbf{I}_{\mathcal{E}_A}$ (43), $\mathbf{I}_{\mathcal{E}_\Phi}$ (44), and $\mathbf{I}_{\mathcal{M}}$ (45) can be evaluated in terms of $\boldsymbol{\xi}'$ on the n_s surfaces where $\mathbf{n} \cdot \mathbf{e}_y \neq 0$. From Table 1, $(\partial \mathbf{x} / \partial \boldsymbol{\xi})_j$ is constant, and $|\partial \mathbf{x} / \partial \boldsymbol{\xi}|_j = 1$. Therefore,

$$\begin{aligned} \mathbf{I}_{\mathcal{E}_A}(\mathbf{x}) &= \sum_{n=0}^{n_m} \tilde{G}_n \int_{S'} R(\mathbf{x}, \mathbf{x}')^{2n} \mathbf{J}_{\text{MS}}(\mathbf{x}') dS' \\ &= \sum_{n=0}^{n_m} \tilde{G}_n \sum_{j=1}^{n_s} \int_0^L \int_{\xi'_{a_j}}^{\xi'_{b_j}} R(\mathbf{x}, \mathbf{x}_j(\boldsymbol{\xi}'))^{2n} J_\xi(\boldsymbol{\xi}') \left| \frac{\partial \mathbf{x}}{\partial \boldsymbol{\xi}} \right|_j \left(\frac{\partial \mathbf{x}}{\partial \boldsymbol{\xi}} \right)_j \mathbf{e}_\xi d\xi' d\eta' \\ &= \sum_{n=0}^{n_m} \tilde{G}_n \sum_{j=1}^{n_s} \left(\frac{\partial \mathbf{x}}{\partial \boldsymbol{\xi}} \right)_j \int_0^L \int_{\xi'_{a_j}}^{\xi'_{b_j}} R(\mathbf{x}, \mathbf{x}_j(\boldsymbol{\xi}'))^{2n} J_\xi(\boldsymbol{\xi}') d\xi' d\eta', \end{aligned} \quad (\text{A.1})$$

$$\begin{aligned} \mathbf{I}_{\mathcal{E}_\Phi}(\mathbf{x}) &= -2 \sum_{n=1}^{n_m} n \tilde{G}_n \int_{S'} R^{2(n-1)} \nabla' \cdot \mathbf{J}_{\text{MS}}(\mathbf{x}') \mathbf{R} dS' \\ &= -2 \sum_{n=1}^{n_m} n \tilde{G}_n \sum_{j=1}^{n_s} \int_0^L \int_{\xi'_{a_j}}^{\xi'_{b_j}} R(\mathbf{x}, \mathbf{x}_j(\boldsymbol{\xi}'))^{2(n-1)} \frac{\partial J_\xi}{\partial \boldsymbol{\xi}}(\boldsymbol{\xi}') \mathbf{R}(\mathbf{x}, \mathbf{x}_j(\boldsymbol{\xi}')) \left| \frac{\partial \mathbf{x}}{\partial \boldsymbol{\xi}} \right|_j d\xi' d\eta' \\ &= -2 \sum_{n=1}^{n_m} n \tilde{G}_n \sum_{j=1}^{n_s} \int_0^L \int_{\xi'_{a_j}}^{\xi'_{b_j}} R(\mathbf{x}, \mathbf{x}_j(\boldsymbol{\xi}'))^{2(n-1)} \frac{\partial J_\xi}{\partial \boldsymbol{\xi}}(\boldsymbol{\xi}') \mathbf{R}(\mathbf{x}, \mathbf{x}_j(\boldsymbol{\xi}')) d\xi' d\eta', \end{aligned} \quad (\text{A.2})$$

$$\begin{aligned} \mathbf{I}_{\mathcal{M}}(\mathbf{x}) &= -2 \sum_{n=1}^{n_m} n \tilde{G}_n \int_{S'} R^{2(n-1)} \mathbf{J}_{\text{MS}}(\mathbf{x}') \times \mathbf{R} dS' \\ &= -2 \sum_{n=1}^{n_m} n \tilde{G}_n \sum_{j=1}^{n_s} \int_0^L \int_{\xi'_{a_j}}^{\xi'_{b_j}} R(\mathbf{x}, \mathbf{x}_j(\boldsymbol{\xi}'))^{2(n-1)} J_\xi(\boldsymbol{\xi}') \mathbf{e}_\xi \times \mathbf{R}(\mathbf{x}, \mathbf{x}_j(\boldsymbol{\xi}')) \left| \frac{\partial \mathbf{x}}{\partial \boldsymbol{\xi}} \right|_j d\xi' d\eta' \\ &= -2 \sum_{n=1}^{n_m} n \tilde{G}_n \sum_{j=1}^{n_s} \int_0^L \int_{\xi'_{a_j}}^{\xi'_{b_j}} R(\mathbf{x}, \mathbf{x}_j(\boldsymbol{\xi}'))^{2(n-1)} J_\xi(\boldsymbol{\xi}') \mathbf{e}_\xi \times \mathbf{R}(\mathbf{x}, \mathbf{x}_j(\boldsymbol{\xi}')) d\xi' d\eta', \end{aligned} \quad (\text{A.3})$$

where $\zeta' = 0$ in $\boldsymbol{\xi}'$, and the directions of $\mathbf{I}_{\mathcal{E}_A}^n$, $\mathbf{I}_{\mathcal{E}_\Phi}^n$, and $\mathbf{I}_{\mathcal{M}}^n$ remain expressed in the \mathbf{x} -coordinate system.

In (A.1)–(A.3), we can replace \mathbf{x} with $\mathbf{x}_j(\boldsymbol{\xi})$, such that

$$\mathbf{R}(\mathbf{x}, \mathbf{x}_j(\boldsymbol{\xi}')) = \mathbf{x}_j(\boldsymbol{\xi}) - \mathbf{x}_j(\boldsymbol{\xi}') = \left(\frac{\partial \mathbf{x}}{\partial \boldsymbol{\xi}} \right)_j (\boldsymbol{\xi}_j - \boldsymbol{\xi}'), \quad (\text{A.4})$$

and

$$R(\mathbf{x}_j(\boldsymbol{\xi}), \mathbf{x}_j(\boldsymbol{\xi}'))^2 = \|\mathbf{R}(\mathbf{x}, \mathbf{x}_j(\boldsymbol{\xi}'))\|_2^2 = \left\| \left(\frac{\partial \mathbf{x}}{\partial \boldsymbol{\xi}} \right)_j (\boldsymbol{\xi}_j - \boldsymbol{\xi}') \right\|_2^2 = \|\boldsymbol{\xi}_j - \boldsymbol{\xi}'\|_2^2. \quad (\text{A.5})$$

Accounting for (A.5), R^{2n} in (A.1) can be written as

$$R^{2n} = \sum_{m=0}^n \sum_{k=0}^m \binom{n}{m} \binom{m}{k} (\xi_j - \xi')^{2(n-m)} (\eta_j - \eta')^{2(m-k)} (\zeta_j - \zeta')^{2k}, \quad (\text{A.6})$$

and $R^{2(n-1)}$ in (A.2) and (A.3) can be written as

$$R^{2(n-1)} = \sum_{m=0}^{n-1} \sum_{k=0}^m \binom{n-1}{m} \binom{m}{k} (\xi_j - \xi')^{2(n-m-1)} (\eta_j - \eta')^{2(m-k)} (\zeta_j - \zeta')^{2k}, \quad (\text{A.7})$$

where $\boldsymbol{\xi}_j = \boldsymbol{\xi}_j(\mathbf{x})$.

Inserting (A.6) into (A.1) and inserting (A.7) and (A.4) into (A.2) and (A.3), (A.1)–(A.3) become

$$\begin{aligned}\mathbf{I}_{\mathcal{E}_A}(\mathbf{x}) &= \sum_{j=1}^{n_s} \sum_{n=0}^{n_m} \sum_{m=0}^n \sum_{k=0}^m \tilde{G}_n \binom{n}{m} \binom{m}{k} \left(\frac{\partial \mathbf{x}}{\partial \boldsymbol{\xi}} \right)_j \mathbf{I}_{\mathbf{J}}^j(\boldsymbol{\xi}_j; 2(n-m), 2(m-k), 2k), \\ \mathbf{I}_{\mathcal{E}_\Phi}(\mathbf{x}) &= -2 \sum_{j=1}^{n_s} \sum_{n=1}^{n_m} \sum_{m=0}^{n-1} \sum_{k=0}^m n \tilde{G}_n \binom{n-1}{m} \binom{m}{k} \left(\frac{\partial \mathbf{x}}{\partial \boldsymbol{\xi}} \right)_j \mathbf{I}_{\nabla', \mathbf{J}}^j(\boldsymbol{\xi}_j; 2(n-m-1), 2(m-k), 2k), \\ \mathbf{I}_{\mathcal{M}}(\mathbf{x}) &= -2 \sum_{j=1}^{n_s} \sum_{n=1}^{n_m} \sum_{m=0}^{n-1} \sum_{k=0}^m n \tilde{G}_n \binom{n-1}{m} \binom{m}{k} \left(\frac{\partial \mathbf{x}}{\partial \boldsymbol{\xi}} \right)_j (\mathbf{e}_\xi \times \mathbf{I}_{\mathbf{J}}^j(\boldsymbol{\xi}_j; 2(n-m-1), 2(m-k), 2k)),\end{aligned}$$

where

$$\mathbf{I}_{\nabla', \mathbf{J}}^j(\boldsymbol{\xi}; p, q, r) = \begin{pmatrix} I_{\nabla', \mathbf{J}}^j(\boldsymbol{\xi}; p+1, q, r) \\ I_{\nabla', \mathbf{J}}^j(\boldsymbol{\xi}; p, q+1, r) \\ I_{\nabla', \mathbf{J}}^j(\boldsymbol{\xi}; p, q, r+1) \end{pmatrix}, \quad \mathbf{I}_{\mathbf{J}}^j(\boldsymbol{\xi}; p, q, r) = \begin{pmatrix} I_{\mathbf{J}}^j(\boldsymbol{\xi}; p+1, q, r) \\ I_{\mathbf{J}}^j(\boldsymbol{\xi}; p, q+1, r) \\ I_{\mathbf{J}}^j(\boldsymbol{\xi}; p, q, r+1) \end{pmatrix}.$$

The directions of $\mathbf{I}_{\nabla', \mathbf{J}}^j$, \mathbf{e}_ξ and $\mathbf{I}_{\mathbf{J}}^j$ are expressed in the $\boldsymbol{\xi}$ -coordinate system, and

$$I_{\mathbf{J}}^j(\boldsymbol{\xi}; p, q, r) = \int_0^L \int_{\xi_{a_j}'}^{\xi_{b_j}'} (\xi - \xi')^p (\eta - \eta')^q (\zeta - \zeta')^r J_\xi(\boldsymbol{\xi}') d\xi' d\eta', \quad (\text{A.8})$$

$$I_{\nabla', \mathbf{J}}^j(\boldsymbol{\xi}; p, q, r) = \int_0^L \int_{\xi_{a_j}'}^{\xi_{b_j}'} (\xi - \xi')^p (\eta - \eta')^q (\zeta - \zeta')^r \frac{\partial J_\xi}{\partial \boldsymbol{\xi}}(\boldsymbol{\xi}') d\xi' d\eta'. \quad (\text{A.9})$$

Recalling that $\zeta' = 0$ in $\boldsymbol{\xi}'$, for $J(\boldsymbol{\xi}) = J_0 \sin(\beta\xi/L) \sin^3(\pi\eta/L)$ (46), (A.8) and (A.9) become

$$\begin{aligned}I_{\mathbf{J}}^j(\boldsymbol{\xi}; p, q, r) &= J_0 \zeta^r \left(\int_{\xi_{a_j}'}^{\xi_{b_j}'} (\xi - \xi')^p \sin\left(\frac{\beta\xi'}{L}\right) d\xi' \right) \left(\int_0^L (\eta - \eta')^q \sin^3\left(\frac{\pi\eta'}{L}\right) d\eta' \right) = J_0 I_p^j(\xi) I_q(\eta) I_r(\zeta), \\ I_{\nabla', \mathbf{J}}^j(\boldsymbol{\xi}; p, q, r) &= \frac{\beta J_0 \zeta^r}{L} \left(\int_{\xi_{a_j}'}^{\xi_{b_j}'} (\xi - \xi')^p \cos\left(\frac{\beta\xi'}{L}\right) d\xi' \right) \left(\int_0^L (\eta - \eta')^q \sin^3\left(\frac{\pi\eta'}{L}\right) d\eta' \right) = \frac{\beta J_0 I_p^j(\xi) I_q(\eta) I_r(\zeta)}{L}.\end{aligned}$$

where $\xi_{a_j}' = \xi_{a_j}$ and $\xi_{b_j}' = \xi_{b_j}$ in Table 1, and

$$I_p^j(\xi) = \int_{\xi_{a_j}'}^{\xi_{b_j}'} (\xi - \xi')^p \sin\left(\frac{\beta\xi'}{L}\right) d\xi' = \sum_{p'=0}^p \binom{p}{p'} (-1)^{p'} \xi^{p-p'} \int_{\xi_{a_j}'}^{\xi_{b_j}'} \xi'^{p'} \sin\left(\frac{\beta\xi'}{L}\right) d\xi' = \sum_{p'=0}^p \binom{p}{p'} (-1)^{p'} \xi^{p-p'} I_{p'}^j,$$

$$I_p^j(\xi) = \int_{\xi_{a_j}'}^{\xi_{b_j}'} (\xi - \xi')^p \cos\left(\frac{\beta\xi'}{L}\right) d\xi' = \sum_{p'=0}^p \binom{p}{p'} (-1)^{p'} \xi^{p-p'} \int_{\xi_{a_j}'}^{\xi_{b_j}'} \xi'^{p'} \cos\left(\frac{\beta\xi'}{L}\right) d\xi' = \sum_{p'=0}^p \binom{p}{p'} (-1)^{p'} \xi^{p-p'} I_{p'}^j,$$

$$I_q(\eta) = \int_0^L (\eta - \eta')^q \sin^3\left(\frac{\pi\eta'}{L}\right) d\eta' = \sum_{q'=0}^q \binom{q}{q'} (-1)^{q'} \eta^{q-q'} \int_0^L \eta'^{q'} \sin^3\left(\frac{\pi\eta'}{L}\right) d\eta' = \sum_{q'=0}^q \binom{q}{q'} (-1)^{q'} \eta^{q-q'} I_{q'},$$

$$I_r(\zeta) = \zeta^r,$$

and

$$\begin{aligned}
I_{p'}^j &= \int_{\xi_{a_j}'}^{\xi_{b_j}'} \xi'^{p'} \sin\left(\frac{\beta\xi'}{L}\right) d\xi' \\
&= - \sum_{p''=0}^{p'} \frac{p'!}{(p'-p'')!} \left(\frac{L}{\beta}\right)^{1+p''} \left[\xi_{b_j}'^{p'-p''} \cos\left(\frac{\beta\xi_{b_j}'}{L} + \frac{p''\pi}{2}\right) - \xi_{a_j}'^{p'-p''} \cos\left(\frac{\beta\xi_{a_j}'}{L} + \frac{p''\pi}{2}\right) \right], \\
I_{\bar{p}'}^j &= \int_{\xi_{a_j}'}^{\xi_{b_j}'} \xi'^{p'} \cos\left(\frac{\beta\xi'}{L}\right) d\xi' \\
&= \sum_{p''=0}^{p'} \frac{p'!}{(p'-p'')!} \left(\frac{L}{\beta}\right)^{1+p''} \left[\xi_{b_j}'^{p'-p''} \sin\left(\frac{\beta\xi_{b_j}'}{L} + \frac{p''\pi}{2}\right) - \xi_{a_j}'^{p'-p''} \sin\left(\frac{\beta\xi_{a_j}'}{L} + \frac{p''\pi}{2}\right) \right], \\
I_{q'} &= \int_0^L \eta'^{q'} \sin^3\left(\frac{\pi\eta'}{L}\right) d\eta' \\
&= \frac{q'!}{8} \left(\frac{L}{3\pi}\right)^{1+q'} \left[2\left(-1 + 3^{2+q'}\right) \cos\left(\frac{q'\pi}{2}\right) \right. \\
&\quad \left. + \sum_{q''=0}^{q'} \frac{\pi^{q''}}{q''!} \left(-3^{2+q'} + 3^{q''}\right) \begin{cases} (-1)^{(q''-q'-2)/2} (1 - (-1)^{q''-q'-1}), & \text{for } q' + q'' \text{ even} \\ 0, & \text{for } q' + q'' \text{ odd} \end{cases} \right].
\end{aligned}$$

References

- [1] R. D. Graglia, On the numerical integration of the linear shape functions times the 3-D Green's function or its gradient on a plane triangle, *IEEE Transactions on Antennas and Propagation* 41 (10) (1993) 1448–1455. [doi:10.1109/8.247786](https://doi.org/10.1109/8.247786).
- [2] D. Wilton, S. Rao, A. Glisson, D. Schaubert, O. Al-Bundak, C. Butler, Potential integrals for uniform and linear source distributions on polygonal and polyhedral domains, *IEEE Transactions on Antennas and Propagation* 32 (3) (1984) 276–281. [doi:10.1109/TAP.1984.1143304](https://doi.org/10.1109/TAP.1984.1143304).
- [3] S. Rao, D. Wilton, A. Glisson, Electromagnetic scattering by surfaces of arbitrary shape, *IEEE Transactions on Antennas and Propagation* 30 (3) (1982) 409–418. [doi:10.1109/TAP.1982.1142818](https://doi.org/10.1109/TAP.1982.1142818).
- [4] M. A. Khayat, D. R. Wilton, Numerical evaluation of singular and near-singular potential integrals, *IEEE Transactions on Antennas and Propagation* 53 (10) (2005) 3180–3190. [doi:10.1109/TAP.2005.856342](https://doi.org/10.1109/TAP.2005.856342).
- [5] P. W. Fink, D. R. Wilton, M. A. Khayat, Simple and efficient numerical evaluation of near-hypersingular integrals, *IEEE Antennas and Wireless Propagation Letters* 7 (2008) 469–472. [doi:10.1109/LAWP.2008.2000788](https://doi.org/10.1109/LAWP.2008.2000788).
- [6] M. A. Khayat, D. R. Wilton, P. W. Fink, An improved transformation and optimized sampling scheme for the numerical evaluation of singular and near-singular potentials, *IEEE Antennas and Wireless Propagation Letters* 7 (2008) 377–380. [doi:10.1109/LAWP.2008.928461](https://doi.org/10.1109/LAWP.2008.928461).
- [7] F. Vipiana, D. R. Wilton, Optimized numerical evaluation of singular and near-singular potential integrals involving junction basis functions, *IEEE Transactions on Antennas and Propagation* 59 (1) (2011) 162–171. [doi:10.1109/TAP.2010.2090464](https://doi.org/10.1109/TAP.2010.2090464).
- [8] F. Vipiana, D. R. Wilton, Numerical evaluation via singularity cancellation schemes of near-singular integrals involving the gradient of Helmholtz-type potentials, *IEEE Transactions on Antennas and Propagation* 61 (3) (2013) 1255–1265. [doi:10.1109/TAP.2012.2227922](https://doi.org/10.1109/TAP.2012.2227922).

- [9] M. M. Botha, A family of augmented Duffy transformations for near-singularity cancellation quadrature, *IEEE Transactions on Antennas and Propagation* 61 (6) (2013) 3123–3134. doi:[10.1109/TAP.2013.2252137](https://doi.org/10.1109/TAP.2013.2252137).
- [10] J. Rivero, F. Vipiana, D. R. Wilton, W. A. Johnson, Hybrid integration scheme for the evaluation of strongly singular and near-singular integrals in surface integral equations, *IEEE Transactions on Antennas and Propagation* 67 (10) (2019). doi:[10.1109/TAP.2019.2920333](https://doi.org/10.1109/TAP.2019.2920333).
- [11] F. Vipiana, D. R. Wilton, W. A. Johnson, Advanced numerical schemes for the accurate evaluation of 4-D reaction integrals in the method of moments, *IEEE Transactions on Antennas and Propagation* 61 (11) (2013) 5559–5566. doi:[10.1109/TAP.2013.2277864](https://doi.org/10.1109/TAP.2013.2277864).
- [12] A. G. Polimeridis, F. Vipiana, J. R. Mosig, D. R. Wilton, DIRECTFN: Fully numerical algorithms for high precision computation of singular integrals in Galerkin SIE methods, *IEEE Transactions on Antennas and Propagation* 61 (6) (2013) 3112–3122. doi:[10.1109/TAP.2013.2246854](https://doi.org/10.1109/TAP.2013.2246854).
- [13] D. R. Wilton, F. Vipiana, W. A. Johnson, Evaluation of 4-D reaction integrals in the method of moments: Coplanar element case, *IEEE Transactions on Antennas and Propagation* 65 (5) (2017) 2479–2493. doi:[10.1109/TAP.2017.2677916](https://doi.org/10.1109/TAP.2017.2677916).
- [14] J. Rivero, F. Vipiana, D. R. Wilton, W. A. Johnson, Evaluation of 4-D reaction integrals via double application of the divergence theorem, *IEEE Transactions on Antennas and Propagation* 67 (2) (2019) 1131–1142. doi:[10.1109/TAP.2018.2882589](https://doi.org/10.1109/TAP.2018.2882589).
- [15] B. A. Freno, W. A. Johnson, B. F. Zinser, D. F. Wilton, F. Vipiana, S. Campione, Characterization and integration of the singular test integrals in the method-of-moments implementation of the electric-field integral equation, *Engineering Analysis with Boundary Elements* 124 (2021) 185–193. doi:[10.1016/j.enganabound.2020.12.015](https://doi.org/10.1016/j.enganabound.2020.12.015).
- [16] P. J. Roache, *Verification and Validation in Computational Science and Engineering*, Hermosa Publishers, 1998.
- [17] P. Knupp, K. Salari, *Verification of Computer Codes in Computational Science and Engineering*, Chapman & Hall/CRC, 2002. doi:[10.1201/9781420035421](https://doi.org/10.1201/9781420035421).
- [18] W. L. Oberkampf, C. J. Roy, *Verification and Validation in Scientific Computing*, Cambridge University Press, 2010. doi:[10.1017/cbo9780511760396](https://doi.org/10.1017/cbo9780511760396).
- [19] P. J. Roache, Code verification by the method of manufactured solutions, *Journal of Fluids Engineering* 124 (1) (2001) 4–10. doi:[10.1115/1.1436090](https://doi.org/10.1115/1.1436090).
- [20] H. Nishikawa, Analytical formulas for verification of aerodynamic force and moment computations, *Journal of Computational Physics* 466 (2022). doi:[10.1016/j.jcp.2022.111408](https://doi.org/10.1016/j.jcp.2022.111408).
- [21] C. J. Roy, C. C. Nelson, T. M. Smith, C. C. Ober, Verification of Euler/Navier–Stokes codes using the method of manufactured solutions, *International Journal for Numerical Methods in Fluids* 44 (6) (2004) 599–620. doi:[10.1002/flid.660](https://doi.org/10.1002/flid.660).
- [22] R. B. Bond, C. C. Ober, P. M. Knupp, S. W. Bova, Manufactured solution for computational fluid dynamics boundary condition verification, *AIAA Journal* 45 (9) (2007) 2224–2236. doi:[10.2514/1.28099](https://doi.org/10.2514/1.28099).
- [23] S. Veluri, C. Roy, E. Luke, Comprehensive code verification for an unstructured finite volume CFD code, in: *48th AIAA Aerospace Sciences Meeting Including the New Horizons Forum and Aerospace Exposition*, American Institute of Aeronautics and Astronautics, 2010. doi:[10.2514/6.2010-127](https://doi.org/10.2514/6.2010-127).
- [24] T. Oliver, K. Estacio-Hiroms, N. Malaya, G. Carey, Manufactured solutions for the Favre-averaged Navier–Stokes equations with eddy-viscosity turbulence models, in: *50th AIAA Aerospace Sciences Meeting including the New Horizons Forum and Aerospace Exposition*, American Institute of Aeronautics and Astronautics, 2012. doi:[10.2514/6.2012-80](https://doi.org/10.2514/6.2012-80).

- [25] L. Eça, C. M. Klaij, G. Vaz, M. Hoekstra, F. Pereira, On code verification of RANS solvers, *Journal of Computational Physics* 310 (2016) 418–439. doi:10.1016/j.jcp.2016.01.002.
- [26] A. Hennink, M. Tiberga, D. Lathouwers, A pressure-based solver for low-Mach number flow using a discontinuous Galerkin method, *Journal of Computational Physics* 425 (2022). doi:10.1016/j.jcp.2020.109877.
- [27] B. A. Freno, B. R. Carnes, V. G. Weirs, Code-verification techniques for hypersonic reacting flows in thermochemical nonequilibrium, *Journal of Computational Physics* 425 (2021). doi:10.1016/j.jcp.2020.109752.
- [28] É. Chamberland, A. Fortin, M. Fortin, Comparison of the performance of some finite element discretizations for large deformation elasticity problems, *Computers & Structures* 88 (11) (2010) 664 – 673. doi:10.1016/j.compstruc.2010.02.007.
- [29] S. Étienne, A. Garon, D. Pelletier, Some manufactured solutions for verification of fluid–structure interaction codes, *Computers & Structures* 106-107 (2012) 56–67. doi:10.1016/j.compstruc.2012.04.006.
- [30] M. Bukač, G. Fu, A. Seboldt, C. Trenchea, Time-adaptive partitioned method for fluid–structure interaction problems with thick structures, *Journal of Computational Physics* 473 (2023). doi:10.1016/j.jcp.2022.111708.
- [31] A. Veeraragavan, J. Beri, R. J. Gollan, Use of the method of manufactured solutions for the verification of conjugate heat transfer solvers, *Journal of Computational Physics* 307 (2016) 308–320. doi:10.1016/j.jcp.2015.12.004.
- [32] P. T. Brady, M. Herrmann, J. M. Lopez, Code verification for finite volume multiphase scalar equations using the method of manufactured solutions, *Journal of Computational Physics* 231 (7) (2012) 2924–2944. doi:10.1016/j.jcp.2011.12.040.
- [33] S. Lovato, S. L. Toxopeus, J. W. Settels, G. H. Keetels, G. Vaz, Code verification of non-Newtonian fluid solvers for single- and two-phase laminar flows, *Journal of Verification, Validation and Uncertainty Quantification* 6 (2) (2021). doi:10.1115/1.4050131.
- [34] R. G. McClarren, R. B. Lowrie, Manufactured solutions for the p_1 radiation-hydrodynamics equations, *Journal of Quantitative Spectroscopy and Radiative Transfer* 109 (15) (2008) 2590–2602. doi:10.1016/j.jqsrt.2008.06.003.
- [35] P. Tranquilli, L. Ricketson, L. Chacón, A deterministic verification strategy for electrostatic particle-in-cell algorithms in arbitrary spatial dimensions using the method of manufactured solutions, *Journal of Computational Physics* 448 (2022). doi:10.1016/j.jcp.2021.110751.
- [36] J. R. Ellis, C. D. Hall, Model development and code verification for simulation of electrodynamic tether system, *Journal of Guidance, Control, and Dynamics* 32 (6) (2009) 1713–1722. doi:10.2514/1.44638.
- [37] A. Amor-Martin, L. E. Garcia-Castillo, J.-F. Lee, Study of accuracy of a non-conformal finite element domain decomposition method, *Journal of Computational Physics* 429 (2021). doi:10.1016/j.jcp.2020.109989.
- [38] A. M. Rueda-Ramírez, F. J. Hindenlang, J. Chan, G. J. Gassner, Entropy-stable Gauss collocation methods for ideal magneto-hydrodynamics, *Journal of Computational Physics* 475 (2023). doi:10.1016/j.jcp.2022.111851.
- [39] A. J. Amar, B. F. Blackwell, J. R. Edwards, One-dimensional ablation using a full Newton’s method and finite control volume procedure, *Journal of Thermophysics and Heat Transfer* 22 (1) (2008) 71–82. doi:10.2514/1.29610.

- [40] A. J. Amar, B. F. Blackwell, J. R. Edwards, Development and verification of a one-dimensional ablation code including pyrolysis gas flow, *Journal of Thermophysics and Heat Transfer* 23 (1) (2009) 59–71. doi:10.2514/1.36882.
- [41] A. Amar, N. Calvert, B. Kirk, Development and verification of the charring ablating thermal protection implicit system solver, in: 49th AIAA Aerospace Sciences Meeting including the New Horizons Forum and Aerospace Exposition, 2011. doi:10.2514/6.2011-144.
- [42] B. A. Freno, B. R. Carnes, N. R. Matula, Nonintrusive manufactured solutions for ablation, *Physics of Fluids* 33 (1) (2021). doi:10.1063/5.0037245.
- [43] B. A. Freno, B. R. Carnes, V. E. Brunini, N. R. Matula, Nonintrusive manufactured solutions for non-decomposing ablation in two dimensions, *Journal of Computational Physics* 463 (2022). doi:10.1016/j.jcp.2022.111237.
- [44] R. G. Marchand, The method of manufactured solutions for the verification of computational electromagnetic codes, PhD dissertation, Stellenbosch (Mar. 2013).
- [45] R. G. Marchand, D. B. Davidson, Verification of the method-of-moment codes using the method of manufactured solutions, *IEEE Transactions on Electromagnetic Compatibility* 56 (4) (2014) 835–843. doi:10.1109/TEMC.2014.2325826.
- [46] B. A. Freno, N. R. Matula, W. A. Johnson, Manufactured solutions for the method-of-moments implementation of the electric-field integral equation, *Journal of Computational Physics* 443 (2021). doi:10.1016/j.jcp.2021.110538.
- [47] B. A. Freno, N. R. Matula, J. I. Owen, W. A. Johnson, Code-verification techniques for the method-of-moments implementation of the electric-field integral equation, *Journal of Computational Physics* 451 (2022). doi:10.1016/j.jcp.2021.110891.
- [48] B. A. Freno, N. R. Matula, Code-verification techniques for the method-of-moments implementation of the magnetic-field integral equation, *Journal of Computational Physics* 478 (2023). doi:10.1016/j.jcp.2023.111959.
- [49] B. A. Freno, W. A. Johnson, B. F. Zinser, S. Campione, Symmetric triangle quadrature rules for arbitrary functions, *Computers & Mathematics with Applications* 79 (2020). doi:10.1016/j.camwa.2019.12.021.
- [50] R. F. Harrington, *Time-Harmonic Electromagnetic Fields*, Wiley–IEEE Press, 2001. doi:10.1109/9780470546710.
- [51] W. C. Chew, *Waves and Fields in Inhomogenous Media*, Wiley–IEEE Press, 1995. doi:10.1109/9780470547052.
- [52] C. A. Balanis, *Advanced Engineering Electromagnetics*, John Wiley & Sons, Inc., 2012.
- [53] W. Chew, J. Jin, E. Michielssen, J. Song, *Fast and Efficient Algorithms in Computational Electromagnetics*, Artech House, 2001.
- [54] P. Ylä-Oijala, M. Taskinen, Calculation of CFIE impedance matrix elements with RWG and $\mathbf{n} \times$ RWG functions, *IEEE Transactions on Antennas and Propagation* 51 (8) (2003) 1837–1846. doi:10.1109/TAP.2003.814745.
- [55] K. F. Warnick, *Numerical Analysis for Electromagnetic Integral Equations*, Artech House, 2008.
- [56] J. N. Lyness, D. Jespersen, Moderate degree symmetric quadrature rules for the triangle, *IMA Journal of Applied Mathematics* 15 (1) (1975) 19–32. doi:10.1093/imamat/15.1.19.
- [57] D. A. Dunavant, High degree efficient symmetrical Gaussian quadrature rules for the triangle, *International Journal for Numerical Methods in Engineering* 21 (6) (1985) 1129–1148. doi:10.1002/nme.1620210612.

- [58] S.-A. Papanicolopoulos, Computation of moderate-degree fully-symmetric cubature rules on the triangle using symmetric polynomials and algebraic solving, *Computers & Mathematics with Applications* 69 (7) (2015) 650–666. [doi:10.1016/j.camwa.2015.02.014](https://doi.org/10.1016/j.camwa.2015.02.014).